# Intrashelf basin record of redox and productivity changes along the Arabian margin of Neo-Tethys during Oceanic Anoxic Event 1a

Arman Jafarian[a], Antun Husinec[b], Chengshan Wang[a*], Xi Chen[a], Meng Wang[c,d], Darren R. Gröcke[e], Abdus Saboor[a,f], Yalin Li[a]

[a] State Key Laboratory of Biology and Environmental Geology, China University of Geosciences, Beijing 100083

[b] Department of Geology, St. Lawrence University, Canton, New York 13617, USA

[c] State Key Laboratory of Desert and Oasis Ecology, Xinjiang Institute of Ecology and Geography, Chinese Academy of Sciences, Urumqi 830011, China

[d]University of Chinese Academy of Sciences, Beijing 100049, China

[e] Department of Earth Sciences, Durham University, South Road, Durham, County Durham, DH1 3LE, UK

[f] Department of Geology, University of Peshawar, Peshawar, 25120, Pakistan

*** Corresponding author:** C. Wang (chshwang@cugb.edu.cn)

## ABSTRACT

The biotic, environmental, climatic, oceanic, and sea-level perturbations during the Early Aptian Oceanic Anoxic Event (OAE) 1a have been extensively documented from both deep- and shallow-marine deposits worldwide. However, there has been relatively little comparative assessment of the simultaneous interplay among organic carbon burial, redox conditions, terrigenous output, and productivity, leading to a lack of precise constraints on these relationships. Here, we use analyses of stable carbon isotopes ($\delta^{13}C_{org}$, $\delta^{13}C_{carb}$, and $\Delta^{13}C$), total organic carbon (TOC), detrital proxies (Al, Si, Ti, K), redox-sensitive (RSTE: U, V, Mo) and productive-sensitive (PSTE: P, Cu, Ni) trace elements from a continuous, predominantly carbonate succession of the Kazhdumi Intrashelf Basin to evaluate the culprits for the OAE1a-associated changes in bottom-water oxygenation, organic-rich layer formation, and biotic shifts along the Arabian margin of the Neo-Tethys. Concentrations of Al-normalized RSTE and TOC values indicate that the bottom water conditions ranged from oxic prior to and at the onset of the OAE 1a (carbon-isotope segments C2 to basalmost C4 *sensu* Menegatti et al., 1998), to anoxic-suboxic but not euxinic (Mo<25 ppm) during the lower C4 through C5+C6 segments, and then returned to oxic-suboxic in the remaining C5+C6 segment. The increase in Al-normalized PSTE coupled with TOC concentrations in the basal C4 is coeval with a change from predominantly orbitolinid-ostreid to planktic foraminifera-radiolarian biota. The periodically high productivity, driven both by the surface-water productivity as well as by phosphorus recycling from the sediments, continued through the C5+C6 segments as evidenced by matching Si/Al and PSTE peaks (Cu/Al and Ni/Al). The study sheds new light on the causes of variations in bottom water deoxygenation, organic content, nutrient availability, and biotic shifts in semi-restricted, relatively deep (>100 m), continental-margin basins during major oceanic perturbations.

**KEYWORDS:** Kazhdumi Intrashelf Basin; High-resolution isotopic curve; Redox and productivity sensitive trace elements; OAE 1a

## 1. Introduction

The Early Aptian oceanic anoxic event (OAE1a, ~120 Ma) was a brief episode (1 to 1.3 Myr duration; Li et al., 2008) of widespread oxygen deficiency of the ocean bottom-waters that resulted in an extensive organic carbon sequestration in marine sediments (Schlanger and Jenkyns, 1976; Arthur et al., 1990). The event is globally recognized by its carbon-isotope signature that is commonly subdivided into distinctive segments (Menegatti et al., 1998; Gröcke et al., 1999; Gröcke, 2002; Castro et al., 2021; Percival et al., 2021), and is defined by a major negative carbon-isotope excursion (segment C3) followed by two pronounced positive excursions (C4 and C6), and post-OAE 1a continuation of high $\delta^{13}C$ values (C7) (Schlanger and Jenkyns, 1976; Arthur et al., 1990; Menegatti et al., 1998; Castro et al., 2021). The major OAE 1a culprit was the flood basalt volcanism associated with the formation of the Greater Ontong Java Plateau, which resulted in a massive release of isotopically light carbon into the atmosphere and the ocean and triggered global warming (e.g., Tarduno et al., 1991; Tejada et al., 2009; Charbonnier and Föllmi, 2017; Matsumoto et al., 2022). Other possible mechanisms include rapid methane release and High Arctic Large Igneous Province (HALIP) sill intrusions into organic-rich marine sediments (e.g., Beerling et al., 2002; Adloff et al., 2020). The massive carbon emissions potentially increased the planetary $pCO_2$

by 3000 ppm (Beerling et al., 2002; Bauer et al., 2017) and arguably led to ocean acidification that resulted in a significant decrease in pelagic biogenic calcite production (Erba, 2004; Erba et al., 2015; see also Gibbs et al., 2011). The Aptian (super)greenhouse conditions were interspersed with cooling events (Jenkyns, 2018) that left a global record of significant sea-level fluctuations (e.g., Matthews and Frohlich, 2002; Husinec and Jelaska, 2006; Graziano et al., 2016; Simmons et al., 2020; Bover-Arnal., 2022), likely driven by aquifer- and glacio-eustasy (Sames et al., 2020). Rapid oceanic deoxygenation (<30 kyr interval)  developed with the onset of OAE 1a (Bauer et al., 2021; carbon-isotope segment C3) following the initial phases of large igneous province volcanism and biological crises, and well before intensified weathering that is recorded in oceanic chemistry 150-300 kyr later (Lechler et al., 2015). Large swaths of the ocean became ferruginous and anoxic for >1 Myr, the latter at least transiently into the photic zone, which resulted in increased rates of trace-metal transfer to the sediment (Algeo, 2004; Algeo and Rowe, 2012) and enhanced pyrite and sulfurized organic matter burial (Bauer et al., 2022). Given the relatively short duration of the OAE 1a, the drawdown of trace elements was of limited duration, and as the event terminated their concentrations in seawater likely recovered rapidly according to their seawater residence times (~730 kyr for Mo, ~400 kyr for U, ~50 kyr for V, and shorter for other metals; Algeo, 2004).

While the environmental, climatic, and biotic impacts of the OAE 1a-associated perturbations on deep- and shallow-water marine carbonate succession have been extensively studied worldwide (e.g., Weissert et al., 1998; Huck et al., 2010; Husinec et al., 2012; Amodio and Weissert, 2017; Hueter et al., 2019; Steuber et al., 2022), the relationship between organic carbon burial, redox conditions, terrigenous input, and productivity remains poorly constrained. Carbonates precipitated in equilibrium with seawater incorporate trace elements and stable isotopes whose values reflect the composition of the ambient seawater (Brand and Veizer, 1980). Following their deposition, however, they commonly underwent a complex series of marine, meteoric, and burial diagenetic processes that altered their original trace element and stable isotope values and shifted them towards equilibrium with the ambient interstitial water (e.g., Brand and Veizer, 1980; Swart and Kennedy, 2012). These processes, whether intrinsic (e.g., mineralogy, porosity, and permeability) or extrinsic (e.g., climate, bioturbation, and advecting fluid composition and flow rate) are primarily influenced by the reactivity of the sediment, the duration of reaction, and the degree of isotopic or elemental/chemical disequilibrium (Fantle et al., 2020). Here, we reconstruct the palaeoredox and paleoproductivity changes across the OAE 1a by utilizing a continuous carbonate sedimentary record from the Kazhdumi Intrashelf Basin exposed in Fars Province (Iran). Given their predominantly mud-supported textures with limited porosity/permeability, and lack of evidence for subaerial exposure in the study area (Jafarian et al., 2023), the potential for an extensive diagenetic modification of the Kazhdumi Intrashelf Basin carbonate sediments was limited. We establish multiple geochemical records, including carbon isotopes ($\delta^{13}C_{org}$, $\delta^{13}C_{carb}$, and $\Delta^{13}C$), total organic carbon (TOC), lithogenic elements (aluminum-Al, silica-Si, titanium-Ti, potassium-K), redox-sensitive trace elements (RSTE; uranium-U, vanadium-V, molybdenum-Mo), and productive-sensitive trace elements (PSTE; copper-Cu, nickel-Ni, phosphorus-P) to unravel the causes of variations in bottom-water deoxygenation, organic-rich layer formation, and biotic shifts taking place in semi-restricted, relatively deep (>100 m), continental-margin basins during major oceanic perturbations.

## 2. Zagros Mountains and the Aptian Kazhdumi Intrashelf Basin

Spanning about 2000 km from the Turkish-Iranian border in the northwest to the Makran area in southeastern Iran, the Zagros fold-thrust belt (ZFTB) occupies the northeastern margin of the Arabian Plate (Alavi, 2004). The Zagros Mountains are notable for their abundance of supergiant hydrocarbon fields, making them the most productive fold-thrust belt on a global-scale (e.g., Falcon, 1958; Murris, 1980; Bordenave and Burwood, 1989; Bordenave and Hegre, 2005). The sedimentary evolution of the Zagros Mountains includes three phases (Heydari, 2008): the Persian Platform phase (latest Precambrian-Early Permian), the Arabian Platform phase (Permian-latest Cretaceous), and the Zagros Foreland Basin phase (latest Cretaceous to present). During the Late Pre-Cambrian to the Permian period, the Persian Platform was a comparatively stable continental platform that was submerged under an epeiric sea (Golonka, 2000; Heydari, 2008). In the Early Permian, the platform experienced the separation of several microplates, which are commonly known as the Cimmerian continent. This event resulted in the formation of the Neo-Tethys Ocean (Golonka, 2000; Heydari, 2008). After the formation of the Neo-Tethys Ocean, the Zagros region became integrated with the Arabian Platform. Throughout the Jurassic and Cretaceous, the Arabian Platform occupied the equatorial region and was connected to the northern margin of Africa (Smith et al., 1994). In the Early Cretaceous, the southern margin of the Neo-Tethys bordered the NE passive margin of the Arabian Plate, which was situated approximately 10–15° S of the equator

(Masse et al., 1993; Sharland et al., 2001). During that time, an extensive shallow-water carbonate platform developed with two intrashelf basins, the Bab Basin to the south and southeast, and the Kazhdumi Basin to the northwest (e.g., Piryaei, 2010; Razin et al., 2010; Mehrabi et al., 2015, 2018; Wohlwend et al., 2016; Bahrehvar et al., 2020; Fig. 1A). The development of the intrashelf basins could have resulted from differential thermal subsidence, halokinetic movements linked to the InfraCambrian Hormuz Salt Series, notably in the eastern Persian Gulf, or the reactivation of extensional basement faults like Kazerun and Hendijan faults in the NW Persian Gulf and the onshore areas of the Zagros Basin (e.g., the Dezful Embayment, Izeh Zone, and Lorestan) (e.g., Wrobel-Daveau et al., 2010; Pierson et al., 2010; Mehrabi and Rahimpour-Bonab, 2014). The Arabian Platform phase terminated in the latest Cretaceous as a result of the collision between the Sanandaj-Sirjan microplate and the Arabian Platform (Golonka, 2000). In the course of the Zagros Orogeny, the Arabian Plate eventually collided with the microcontinent of Iran, leading to the closure of the Neo-Tethys Ocean and the formation of the ZFTB (Berberian and King, 1981; Golonka, 2000; Agard et al., 2005). However, the exact timing of the collision remains a subject of debate, with various estimates suggesting a range from the Late Cretaceous to Pliocene (e.g., Stöcklin, 1968; Berberian and King, 1981; Koop and Stoneley, 1982; Fakhari, 2008; Horton et al., 2008).

The Kazhdumi Intrashelf Basin differentiated during the Early Aptian with a maximum water depth estimated at 135 m (van Buchem et al., 2010). The basin was connected with the Neo-Tehys Ocean, which enabled an efficient exchange of waters with the open ocean during the OAE 1a. The biostratigraphy, chemostratigraphy, lithostratigraphy, and facies of the Lower Aptian Lower Dariyan succession are summarized below.

## 2.1. Lithostratigraphy

At its type locality measured at Kuh-e Gadvan (Fars Province, Iran), the Dariyan Formation is comprised of thick-bedded, massive, orbitolinid limestone (James and Wynd, 1965), which was formed in a shallow-marine environment. Except for the central and southern Lurestan, where it grades into shales and limestones of the Garau Formation, the Dariyan Formation is found throughout southwestern Iran (Fig. 1B). On the opposite, the Arabian side of the Persian Gulf, its stratigraphic equivalent is the Shu´aiba Formation. Towards the Kazhdumi Basin margin, the

Dariyan Formation is subdivided into three informal units, including Lower Dariyan, Kazhdumi Tongue (Middle Dariyan), and Upper Dariyan (e.g., van Buchem et al., 2010; Mehrabi et al., 2015, 2018; Jafarian et al., 2023).

In the study area, the 39.5-m-thick Lower Dariyan unit conformably overlies shales, marls, and limestones of the Barremian-Aptian Gadvan Formation, and is conformably overlain by shales and marls of the Kazhdumi Tongue (Middle Dariyan unit) (Fig. 2A–C). The lower part of the lower Dariyan unit is made up of thin- to medium-bedded, predominantly dark-gray, mud-supported skeletal limestones with larger benthic foraminifera, subordinate planktonic foraminifera, and rare ammonite casts, and interbedded with shell beds (ostreid limestone; Fig. 2D). In the middle part of the lower Dariyan unit, which is regionally known as the radiolarian flood zone (RFZ) (James and Wynd, 1965; Vincent et al., 2010), dark gray radiolaria-rich limestones alternate with dark gray shales and black chert bands (laterally discontinuous; up to 12 cm thick). The remaining upper part of the Lower Dariyan unit is made up of mud-supported, radiolarian and planktic foraminiferal limestones. The contact between the Lower Dariyan unit and Kazhdumi Tongue is gradual and characterized by a color change from dark to greenish gray (Fig. 2B–C).

## 2.2. Lower Aptian facies

The Lower Aptian facies and interpreted depositional settings of the Kazhdumi Intrashelf Basin were described in detail by van Buchem et al. (2010), Mehrabi et al. (2015, 2018), Bahrehvar et al. (2020), and Jafarian et al. (2023). In the study area, four distinct microfacies are identified, from deepest to shallowest: radiolarian wackestone and packstone (MF1; Fig. 3A), planktic foraminiferal wackestone and packstone (MF2; Fig. 3B), skeletal wackestone and floatstone (MF3; Fig. 3C), and ostreid packstone and rudstone (MF4; Fig. 3D). The main characteristics of each microfacies are summarized below after Jafarian et al. (2023).

Gray to dark gray radiolarian wackestone and packstone (MF1) is dominated by well-sorted, mostly spherical radiolarians (abundance ~20–40%) in a dark micrite matrix with organic matter. Sponge spicules (mainly monoaxon), echinoid spines, and planktonic foraminifers (mainly *Hedbergella* spp.) are subordinate, whereas coccoliths are rare. This microfacies is thinly bedded, locally laminated, and associated with chert bands. The majority of radiolarian tests are completely filled with sparry calcite. Pyritization and chemical compaction are common. The MF1 microfacies formed in a deep water, distal part of the intrashelf basin. It comprises 45% of the studied section.

Light gray to black, organic-rich planktic foraminiferal wackestone and packstone (MF2) contains predominantly well to moderately sorted planktonic foraminifers (abundance 10–20%; hedbergellids, globigerinelloids and leupoldinids), whereas sponge spicules, pelagic echinoids, bivalve fragments, and radiolarians are subordinate (5–10%). Most skeletal fragments and foraminiferal tests are completely replaced or filled with sparry calcite; pyritization is common. The MF2 microfacies deposited in a low-energy, open-marine setting likely with oxygen-depleted bottom conditions. It makes up ~25% of the studied section.

Skeletal wackestone and floatstone (MF3; corresponds to MF4 of Jafarian et al., 2023) is made up of medium- to fine-grained, poorly sorted allochems (abundance ~15%), including corals, gastropods, echinoid spines, and planktonic foraminifers (rare) along with coarse-grained bivalve fragments (e.g., *Exogyra* sp.) and larger benthic foraminifera (e.g., *Lenticulina* sp., *Choffatella decipiens*, *Palorbitolina lenticularis*) in a micritic matrix. Hematite and pyrite have replaced some of the shells and filled in the molds. The MF3 microfacies deposited in a mid-ramp, low- to moderate-energy setting likely close to the storm wave base. It constitutes 27.5% of the studied section.

Ostreid packstone and rudstone (MF4; corresponds to MF6 of Jafarian et al., 2023) contains poorly sorted, medium- to coarse-sized (≤5 mm; abundance 15–20%) fragments of ostreid bivalves (*Exogyra* sp.) that exhibit normal grading. Other skeletal components (abundance 5–10%) include large benthic foraminifera (e.g., *Lenticulina* sp., *C. decipiens*), echinoderms, gastropods, and serpulids, whereas planktonic foraminifers (*Hedbergella* spp.), echinoid spines, and sponge spicules are rare. Replacement (pyritization, hematitization), boring/burrowing (due to serpulid worm activity), and fracture-filling calcite cementation are the most common diagenetic processes. This microfacies formed in a mid-ramp setting with vigorous sediment reworking during storms. It makes up only 2.5% of the studied section.

### 2.3. Biostratigraphy and chemostratigraphy

The age of the studied Lower Dariyan unit of the Dariyan Formation has been established as Early Aptian (Bedulian) based on benthic foraminiferal, planktic foraminiferal, and ammonite biozones, and tied to carbon-isotope stratigraphy (e.g., Vincent et al., 2010; Schroeder et al., 2010; Yavari et al., 2017; Mehrabi et al., 2018; Jafarian et al., 2023). The lower part of the Lower Dariyan unit contains abundant benthic foraminifera *Palorbitolina lenticularis* and *Choffatella decipiens*, which are typical for the earliest Early Aptian (e.g., Peybernès, 1982; Husinec, 2001; Husinec and Sokač, 2006; Schroeder et al., 2010; Granier et al., 2017; Schlagintweit and Rashidi, 2022). The last appearance of these larger benthic foraminifera is associated with the regional deepening and deposition of the RFZ. In the basin center, the RFZ spans the *Deshayesites weissi* to *Deshayesites deshayesi* ammonite zones (Vincent et al., 2010) and includes the regional K80 maximum flooding surface (Sharland et al., 2001; Mehrabi et al., 2018). The overlying Kazhdumi Tongue unit contains the first appearance datum of *Mesorbitolina parva*, which is indicative of the late Aptian Gargasian (Schroeder et al., 2010; Yavari et al., 2017).

The age of the Lower Dariyan interval at the Dareh Sefid section has further been constrained by chemostratigraphy and tied to carbon-isotope segments *sensu* Menegatti et al. (1998). The C-isotope segments were identified based on the unsmoothed $\delta^{13}$C curve following Menegatti et al. (1998) original definition (Jafarian et al., 2023); the bulk carbonate $\delta^{13}$C values range from -0.8 to +4.6‰ VPDB (mean +1.9‰). The basal part of the unit corresponds to the segment C2, which corresponds to the upper *G. blowi* zone. The remaining Lower Dariyan succession deposited during the OAE 1a (C3–C6) span from the uppermost *Globigerinelloides blowi* into the upper *Leupoldina cabri* zone, with RFZ spanning from the upper C4 to the lower C5 (Jafarian et al., 2023). Segment C2 is characterized by relatively uniform $\delta^{13}$C values, and is followed by a major negative shift (-1.4 to -1.6‰; segment C3) marking the onset of OAE 1a. A subsequent stepwise positive excursion to +2.8‰ VPDB corresponds to segment C4 at the Dareh Sefid section. The remainder of OAE 1a exhibits relatively constant values (C5 + C6), with a pronounced positive shift at the top of this joint segment (Jafarian et al., 2023).

## 3. Methodology

The samples were collected from the Dareh Sefid section (near a small village with the same name; it is also locally known as Banesh due to its proximity to a bigger homonymous village), which crops out NW of Shiraz City, Fars Province (Figs. 1–2). The 265-m-thick section has recently been logged in detail and analyzed for microfacies, biostratigraphy, chemostratigraphy (stable carbon and oxygen), and sequence stratigraphy (Jafarian et al., 2023). In this study, we focused on the 39.5-m-thick lowermost Aptian part of the section, and used additional geochemical analyses of 80 samples collected at 0.5–0.7 m intervals.

Sampling for $\delta^{18}O/\delta^{13}C_{carb}$ isotopes centered on the extraction of powders from the micritic matrix using a microdrill under a reflected-light microscope. The $\delta^{18}O/\delta^{13}C_{carb}$ analysis is described in detail in Jafarian et al. (2023, and their Supplementary Material Table). Given the absence of subaerial exposure and non-depositional emergent episodes, the succession likely contains a complete record of $\delta^{13}C_{carb}$ oscillations (cf., platform carbonates; Husinec and Read, 2018). For the $\delta^{13}C_{org}$ analysis (Table S1), the powdered rock samples were decalcified using 3M HCl (at room temperature) in 50 ml centrifuge tubes for 16 h. Samples were subsequently neutralized with de-ionized water and dried at 40°C for 36 h. The sample pellets were reground and weighed into tin capsules for carbon isotope analysis. Stable isotope measurements were performed at Durham University in the Stable Isotope Biogeochemistry Laboratory (SIBL) using a Costech Elemental Analyzer (ESC4010) coupled to a Thermo Scientific Delta V Advantage isotope ratio mass spectrometer. Carbon isotope ratios are corrected for $^{17}O$ and reported in standard delta (δ) notation in per mil (‰) relative to Vienna Pee Dee Belemnite (VPDB). Isotopic accuracy was monitored through routine analyses of in-house standards and international standards (IAEA-600, IAEA-CH-3, IAEA-CH-6, NBS 19, USGS24, USGS40). International and in-house standards were run daily and provided a linear range of $\delta^{13}C_{org}$ between –46‰ and +3‰ for isotopic correction. Analytical accuracy in sample $\delta^{13}C_{org}$ was better than 0.2‰ (2σ) based on standards and replicate sample analysis.

Total organic carbon (TOC) data (Table S1) were obtained as part of the isotopic analysis using the internal standard, glutamic acid (40.82 wt.% C). The Costech Elemental Analyzer was set to macro-oxygen for complete combustion to liberate all organic carbon. The isotope analyses were done in "no dilution mode" and all analyses produced a $CO_2$ signal > 800 mV, hence providing maximum confidence in the reported $\delta^{13}C_{org}$ values.

Bulk-rock major and trace elements (RSTE = redox-sensitive elements e.g., Mo, U, V and PSTE = productivity-sensitive elements e.g., Cu, Ni, P) were analyzed by X-ray fluorescence

(XRF) and inductively coupled plasma mass spectrometry (ICP-MS) on 40 samples at ALSGLOBAL Laboratory, China (Table S2). To prepare the samples for the XRF analysis, the whole-rock powders (200-mesh) were first dried in an oven for 4 h at 105°C. Then, approximately 0.6 g of each sample powder was mixed with 6 g of lithium borate flux mixture and 0.3 g of oxidant, and a few drops of lithium bromide were added as a release agent. The mixture was then fused in a furnace at 1050°C. The resulting flat glass discs were analyzed using the ZSX Primus II spectrometer. Samples were calibrated according to the Chinese National Reference Materials (GBW07103, GBW07105, GBW07107, GBW07111). Using the theoretical α coefficient method, the data were corrected and yielded a relative standard deviation of < 2 wt. %.

For ICP-MS, 200-mesh samples were dried in an oven at 105 °C for 12 h. Then, 50 mg of each dried sample was precisely weighed and transferred into a Teflon bomb. Following this, 1 ml each of $HNO_3$ and HF were slowly introduced into the Teflon bomb. The Teflon bomb was placed in a stainless steel pressure jacket and heated to 190 °C for > 24 h in the oven. Once cooled, the Teflon bomb was opened and placed on a hotplate at 140°C. The sample was evaporated to incipient dryness and 1 ml $HNO_3$ was added. The sample was then evaporated to dryness again. Next, a solution containing 1 ml of $HNO_3$, 1 ml of MQ water, and 1 ml of 1ppm In internal standard solution was added. The Teflon bomb was released and placed in the oven at 190 °C for > 12 h. Finally, the resulting solution was transferred into a polyethylene bottle, and the volume was adjusted to 100 g by adding 2 $HNO_3$. The Agilent 7700e ICP-MS was utilized to conduct trace element analyses of whole rock samples. Lower detection limits range from 0.01 to 5 ppm. The analytical reproducibility, as determined by performing replicate analyses on selected samples, was found to be < 5%.

To minimize the effects of biogenic/authigenic carbonate enrichment and detrital dilution, selected elements were normalized to aluminum (element/Al), which is the main component of alumosilicate sediment fraction, does not move during diagenesis, and is therefore commonly used for comparison among different units (Tribovillard et al., 2006). Plots showing element/Al ratios used in this study (V/Al, Mo/Al, U/Al, Ni/Al, Cu/Al, P/Al) against the stratigraphic interval, show the level of enrichment or depletion relative to their concentration in a reference, which in this case is an average shale (AS) (Wedepohl, 1971, 1991; Table S3). Both the Al normalization and comparison to AS values have their drawbacks, and should not be used as the only method to quantitatively identify elemental contributions (Van der Weijden, 2002). The triangular $Al_2O_3$ – $SiO_2$ – CaO diagram (Brumsack, 1989) was constructed to evaluate the variability of the three main sedimentary rock components recorded within the studied succession, i.e., clays, quartz and/or biogenic silica, and calcium carbonate. The strengths of association between selected variables were evaluated using the Pearson correlation.

## 4. Results

### 4.1. Organic carbon isotopes ($\delta^{13}C_{org}$) and $\Delta^{13}C$

The $\delta^{13}C_{org}$ values range from -27.2‰ to -22.6‰ (mean= -25.4‰; Table S1; Fig. 4), with the highest value recorded at the base of the RFZ. The basal part of the section (lower C2 segment) shows an increase in values reaching -25.5‰ at ~3 m, which is followed by a decrease to -27.2‰ at ~7 m (upper C2). The values increase across the C2–C3 boundary reaching -26.5‰ at the base of C4. The values remain relatively constant through lower C4, which is followed by a pronounced positive excursion to -22.6‰ at the base of the RFZ. From there, the values exhibit a stepwise decrease to -25.6‰ at 22 m, followed by an increase to -23.8‰ at ~24 m; the latter is correlatable with a positive shift in TOC values in the upper RFZ. The remaining RFZ and Lower Dariyan succession (segments C5+C6) exhibits relatively uniform values (average -24.5‰) with three minor positive excursions at ~32, ~34, and ~37 m.

The isotopic difference between paired isotopic measurements of bulk carbonate and organic matter ($\Delta^{13}C = \delta^{13}C_{carb} - \delta^{13}C_{org}$) ranges from 23.8‰ to 28.4‰ (mean= 27.0‰; Table S1; Fig. 4). The basal part of the section (lower C2 segment) shows a stepwise decrease in values reaching 25.6‰ at ~3 m, which is followed by an interval of relatively uniform values in the upper C2 segment (27.2‰ to 27.5‰). The negative excursion begins with the onset of the OAE 1a (C2–C3 boundary) and reaches the minimum $\Delta^{13}C$ value of 25‰ at the base of C4, which corresponds to the lowest $\delta^{13}C_{carb}$ value (recorded in the section -0.8‰; Fig. 4). This is immediately followed by a positive excursion to 27.64‰ at 11 m and an interval of stepwise, gently increasing values. A major negative excursion at the base of the RFZ (from 28.1‰ to 23.8‰; 5.1‰ shift) is immediately followed by a stepwise positive shift to 28‰ at 20 m in the lower RFZ (= upper C4 segment). The values remain relatively constant (mean= 27‰) towards the middle part of the

C5+C6 segment at 30 m, which is followed by a negative excursion to 25.7‰ at ~34 m, a positive shift to 27% at 36 m, and finally a negative excursion to 25.5‰ on top of the studied interval.

### 4.2. Total organic carbon

TOC values of the studied Lower Dariyan unit are relatively low (mean= 0.8 wt. %) and range from 0.1 to 3.0 wt. % (Table S1, Fig. 4). The highest values are associated with black argillaceous and thin-bedded limestones. Segments C2 and C3 have relatively constant, low TOC values (mostly between 0.2 and 0.4 wt. %; max. 0.9 wt. %). The lower C4 segment (up to the base of RFZ) is characterized by overall increasing values with two prominent positive excursions at ~13 m (2.2 wt. %) and ~17 m (3.0 wt. %). The latter value represents the highest TOC in the section, which is recorded <1 m below the base of the RFZ (Fig. 4). The TOC values of the RFZ then progressively decrease from 0.5 wt. % at 18 m (~middle C5) to 0.4 wt. % at 24 m (basal C5) with a positive excursion to 2.4 wt. % at 23 m. Pronounced, stepwise increase in values characterizes the remaining upper part of the RFZ, with the maximum value of 2.5 wt. % immediately above the RFZ at 27.1 m (lower C5+C6 segment). The upper part of the section exhibits more heterogeneous values with initially decreasing values to 0.2 wt. % at 30 m, which is followed by a stepwise increasing trend to a maximum of 1.9 wt. % at 34 m. After a drop to 0.2 wt. % at 35 m, the remaining part of the section exhibits a gentle stepwise increasing trend with maximum values below 1.3 wt. %.

### 4.3. Major and trace elements

The triangular $Al_2O_3$ – $SiO_2$ – CaO diagram (Fig. 5A) shows that the majority of the samples plot at or below the 'carbonate dilution line', which connects the average shale (AS) point to the pure carbonate end-member and exhibits a tendency towards higher $SiO_2$ contents. The highest $SiO_2$ and the lowest CaO contents are recorded in segments C5+C6, especially in samples from the upper part of the RFZ (Table S2). Only three samples from the top of the studied interval (segment C6) show fair enrichment in Al content ($Al_2O_3$ (x5) content > 20 %; Fig. 5A).

#### 4.3.1. Detrital proxies

The titanium content of the analyzed samples varies from 0.01 to 0.78 wt. % (mean= 0.02 wt. %), with the highest values recorded in the topmost part of the section (upper segment C5+C6); the remaining section generally has much lower Ti values (mean= 0.01 wt. %). The potassium content ranges from 0.02 to 0.25 wt. % (mean= 0.09 wt. %). It mirrors the Ti trend, with the highest values in the same interval (upper segment C5+C6), whereas the remainder of the section has mean K content of 0.07 wt. %. The Si content varies from 0.35 to 13.6 wt. % (mean= 4.8 wt. %), but the values are ~5x greater in segment C5+C6 (7.52 wt. %) compared to segments C2 to C4 (mean= 1.56 wt. %). The above-selected lithogenic elements (Koinig et al., 2003) exhibit strong (Ti; R= +0.98), moderate (K; R= +0.54) to weak (Si; R= +0.44) correlation with Al (wt.%) (Fig. 5B–D). Conversely, linear plots of K, Si, and Ti with Ca (%) indicate a moderate negative correlation between the three elements (Fig. 5E–G).

The Al-normalized values of selected lithogenic elements (Si/Al, Ti/Al, and K/Al) are displayed in Figure 6 and Table S3. The K/Al and Ti/Al values are lower than AS values in the same 2 intervals: 0–12.8 m (Segments C2 to basal C4), and 25.1–38.8 m (C5+C6, excluding its basal part). Within the interval with most values > AS (lower C4 through basal C5+C6), three peaks with the highest values are identified at 14.1 m (lower C4), 17.1 m (middle C4, right below the RFZ), and 20.8 m (basal C5). The highest values below the RFZ base correspond to relatively high TOC (2.58 %), although the highest TOC value (2.96 %) immediately below correlates with low both K/Al and Ti/Al ratios. The Si/Al ratios are similar to slightly above the AS values up until the mid-segment C4, i.e., right below the RFZ. Further up-section, with the exception of three values similar to AS, they are much higher with three peaks showing >10x greater values than AS (at 20.1 m, 23.8 m, and 31.1 m). The remaining upper C5+C6 segment exhibits a gradual return to AS values. In addition, the relatively low values of K, Si, and Ti at 16.8 m (mid-C4) coincide with comparatively high TOC (2.58 %; Fig. 6; Table S3).

#### 4.3.2. Redox- and productive-sensitive trace elements

The selected RSTE (U, V, Mo) and PSTE (Cu, Ni, P) investigated in this study are shown in Table S2, and normalized to Al in Figure 6 and Table S3. U/Al and V/Al values are relatively low from the base of the section to 13.1 m (segments, C2, C3, and basal C4). This is followed by a gradual increase in V/Al to a maximum value of 4130 at 23.1 m (top C4) and a subsequent decrease. The corresponding U/Al values show a stepwise increase to a maximum of 83.8 in the mid-C4, immediately below the base of RFZ; this is followed by a gradual decrease through upper C4 and lower C5+C6. Both U/Al and V/Al show relatively uniform values slightly greater than AS above 23.1 m (above RFZ). Contrary to U/Al and V/Al, the Mo/Al curve is characterized by more fluctuating values with several excursions to values significantly greater than AS (at 7.8 m in segment C2, and 27.8 m and 31.8 m in segment C5+C6). Note that the entire upper part of segment C4 has high Mo/Al values, except for a single low point at 16.8 m (Fig. 6). All three high RSTE values correspond to high TOC at 17.1 m (mid-C4, below the RFZ base) and 23.1 m (top C4). Otherwise, the highest TOC values generally do not match all three (or two) RSTE highs.

Cu/Al and Ni/Al are characterized by low, relatively uniform values in segments C2 and C3 (0–10.8 m), and above 25.1 m (basal C5+C6) (Fig. 6). Both exhibit a smaller peak in lower segment C4, and the highest value around the C4–C5 boundary (Ni/Al= 341.4, Cu/Al= 999.4); Ni/Al also shows a third peak with higher values in mid-C4 below the RFZ. From the base to ~11 m (C2 and C3 segments), there is a consistent decreasing trend observed in the P/Al ratios, with values from 0.2 to 0.05 (mean= 0.11). There are two distinct and prominent peaks in P/Al content, one in basal C4 (0.52) and the other one at 20.8 m in the upper C4 (0.53). Subsequently, the P/Al content in the C5+C6 segment is lower and fluctuates from 0.04 to 0.12, with four minor peaks of up to 29.1; the lowest of these positive excursions occurs at the RFZ top.

## 5. Discussion

### 5.1. Fluctuations in TOC and $\delta^{13}$C and assessment of primary values

The Lower Dariyan TOC values from the studied succession suggest that starting from segment C4, conditions in the Kazhdumi Basin were periodically favorable for the preservation of the organic matter (TOC>1 %), especially immediately preceding and during the RFZ deposition (RFZ values from 4.5 to 9 %; Bordenave and Hegre, 2010). This is within a range of values recorded from the Sub-Briançonnais basinal marls and limestones that deposited along the Iberian continental margin (TOC in segments C2–C6 ranges between 0 and 6 %; Charbonnier et al., 2018), the epicontinental Ionian Basin deposits (TOC also range between 0 and 6 %; Karakitsios, 1995), or from other coeval intrashelf or deep-pelagic basinal sections worldwide (Castro et al., 2021, and references therein). It is important to note, that the organic-rich deposits were geographically restricted and characterized by a diachronous occurrence between different basins and carbonate platforms (e.g., Huck et al., 2010; Föllmi, 2012; Husinec et al., 2012; Mutterlose et al., 2014; Blok et al., 2022).

A moderate to strong relationship (R= +0.66) between $\delta^{13}C_{org}$ and $\delta^{13}C_{carb}$, similar scatter of values (4.6‰ in $\delta^{13}C_{org}$, and 3.7‰ in $\delta^{13}C_{carb}$; Fig. 7A), and no to very week relationship (R= +0.08) between $\delta^{13}C_{org}$ and TOC (Fig. 7B), suggests that the paired primary values are generally preserved albeit likely affected to a certain degree by local environmental processes and diagenesis (cf., Edwards and Saltzman, 2016). Although the Lower Dariyan $\delta^{13}C_{org}$ trends appear to be broadly covariant with $\delta^{13}C_{carb}$, the decoupling in segment C3 and in the middle part of C5+C6 (Fig. 4) suggests that the $\delta^{13}C_{org}$ signal may have periodically been modified by biological or geological processes. This is likely because $\delta^{13}C_{org}$ is commonly subjected to a wide range of factors that can affect its values, such as changing contributions of terrestrial and marine organic carbon, variations in the C-isotopic composition of the dissolved $CO_2$ metabolized by phytoplankton during carbon fixation, changing fractionation of C-isotopes during photosynthesis, and changes in the surface ocean carbon reservoir (e.g., Lini et al., 1992; Sluijs and Dickens, 2012).

The positive shifts in $\delta^{13}C_{org}$ observed in the RFZ (mid-C4 to lower C5+C6), which pair well with the positive shifts in $\delta^{13}C_{carb}$ (Fig. 4), suggest a global increase in the burial rates of organic carbon, potentially leading to falls in atmospheric $pCO_2$ (Kump and Arthur, 1999). The shifts could have been driven by a range of factors, including increased productivity, decreased dissolved $CO_2$ in surface waters, as well as by changes in the organic material sources (Hatch et al., 1987). A significant decrease in $\Delta^{13}C$ values associated with a paired increase in $\delta^{13}C_{org}$ and $\delta^{13}C_{carb}$ in the lower RFZ, suggests that it was likely driven by a productivity increase in surface waters (Patzkowsky et al., 1997), as evidenced by a contemporaneous increase in the abundance of planktonic foraminifera and radiolarians (Jafarian et al., 2023).

The observed paired ($\delta^{13}C_{org}$ and $\delta^{13}C_{carb}$) negative excursions are not the result of a meteoric alteration of $\delta^{13}C_{carb}$ record (cf., Oehlert and Swart, 2014), as suggested by a lack of evidence for subaerial exposure within the studied succession (Jafarian et al., 2023). This is also supported by the lack of correlation on $\delta^{13}C_{org}$ vs. TOC and $\Delta^{13}C_{org}$ vs. TOC cross plots (Fig. 7B, C), as isotopically heavy bulk organic carbon values do not show consistently low TOC related to increased respiration by either biological or geological processes, including thermal degradation of organic matter during burial diagenesis (Popp et al., 1998; Hayes et al., 1999).

## 5.2. Provenance of non-carbonate sediment fraction

The triangular phase diagram ($Al_2O_3$ – $SiO_2$ – CaO; Fig. 5A) supports background sedimentation dominated by benthic and pelagic carbonate skeletal fragments and an increased biogenous silica component due to the abundance of radiolarians and sponge spicules, especially within the RFZ. This is also supported by a simultaneous rise in the abundance of productivity proxies (Cu/Al, Ni/Al, and P/Al; discussed later). The very low Ti/Al, K/Al, and Si/Al values indicate pure carbonate deposition during stages C2, C3, and basalmost C4. Since quartz and heavy minerals are commonly found together in coarser grain-size fractions and are indicative of high-energy environments (e.g., Dellwig et al., 2000), the higher Ti/Al ratios that correspond with increased Si/Al ratios within the lower C4 segment are suggestive of the presence of detrital quartz (Hetzel et al., 2011). The higher $SiO_2$ content within the interbedded shales of the uppermost Lower Dariyan unit (segment C5+C6; Table S2) was due to the presence of biogenous silica, as also suggested by very low Ti/Al and K/Al, and high Si/Al values.

Strong Ti to moderate K positive correlation with Al suggests detrital input of these lithogenic elements, whereas weak Si-Al correlation indicates that the $SiO_2$ source was both biogenous silica and detrital (Fig. 5B–D). Given that the Ti concentration is considered as a proxy for the input of coarse- to medium-grained, and K as a proxy for fine-grained detrital fractions (Gambacorta et al., 2020 and references therein), the strong Ti to moderate K correlation with the fine-grained proxy (Al) suggests an influx of both the coarse- to medium-grained and fine-grained detrital fractions into the basin. Siliciclastic input onto the markedly asymmetrical Lower Cretaceous Arabian Platform was most pronounced during periods marked by concurrent tectonic uplift in the hinterland, humid or seasonally wet climates, and significant eustatic falls (Yose et al., 2006; Davies et al., 2019). Accordingly, the uplift had exposed basement rock types and older sedimentary rocks to weathering and erosion, influencing the slope profile and subsequently affected sediment transport rates to the shelf, which is evidenced by the accumulation of thick sandstone-dominated units (e.g., Zubair and Burgan formations; Davies et al., 2019). In the

Kazhdumi Intrashelf Basin, tectonic control is suggested by the activation of the Kazerun Fault system during the late Early Aptian (van Buchem et al., 2010). In the absence of an exposed siliciclastic area in the vicinity of the basin (Fig. 1), it seems plausible that the very fine siliciclastic detritus was blown in by the wind.

### 5.3. Palaeoredox conditions in the Kazhdumi Intrashelf Basin

RSTE enrichment and their occurrence within the organic-rich sediments are commonly utilized as a proxy for identifying the palaeoredox conditions and the changes thereof during deposition and early diagenesis (Boning et al., 2004; Rimmer, 2004; Brumsack, 2006; Tribovillard et al., 2006). Thus, they reflect redox conditions of bottom waters and/or porewaters close to the sediment water interface (Algeo and Li, 2020). Typically, RSTEs are more soluble under oxidizing conditions and can be removed from the water column to the sediments either by biotic (mainly phytoplankton) or abiotic processes, the latter particularly efficient under reducing conditions (Tribovillard et al., 2006). For instance, in anoxic environments, uranium is reduced and fixed in marine carbonates as insoluble uranous ($U^{4+}$), while in oxidizing conditions uranium ions keep the higher oxidation state ($U^{6+}$) and form uranyl carbonate ($UO_2(CO_3)_3^{4-}$), which is soluble in ambient water. Accordingly, anoxic deposits are normally more U-enriched than oxic sediments (Wignall and Twitchett, 1996). Similar to uranium, Mo and V are also incorporated into the sediments under the reducing conditions, either by precipitation as oxides and hydroxides, by the creation of organo-metal ligands in humic acids, or by surface adsorption (Algeo and Maynard, 2004; Tribovillard et al., 2004). Furthermore, U and V can be reduced and accumulated in the sediments under denitrifying settings (suboxic to anoxic), while Cu, Mo, Ni, and Zn are chiefly enriched under sulfate-reducing environments (i.e., under a more advanced stage of deoxygenation; Tribovillard et al., 2006). Therefore, if U and V are enriched without the concurrent Mo enrichment, then the bottom waters or porewaters were suboxic to anoxic without free hydrogen sulfide ($H_2S$), whereas sediments that show simultaneous enrichments in U, V, and Mo are indicative of anoxic to euxinic conditions either at the sediment-water interface or in the water column (Algeo and Maynard, 2004; Tribovillard et al., 2006). On the basis of our results, the setting was non-euxinic as suggested by, except for two outliers, Mo concentrations <25 ppm (Scott and Lyons, 2012; Table S2). However, as noted by Algeo and Liu (2020), no single proxy should be taken as a universally reliable redox indicator, albeit some are more dependable; in particular, TOC and trace metal enrichment factors.

Lithologically, segments C2 through basalmost C4 are dominated by frequently bioturbated, grayish-white to light gray, medium-to-thick bedded mollusk wackestone-floatstone and packstone-rudstone with ostreids, rudists, benthic foraminifera, echinoids spines, and crinoids (Jafarian et al., 2023). This, coupled with low TOC and low RSTE (Fig. 6; Table S3), suggests well-oxygenated conditions in the Kazhdumi Intrashelf Basin before and at the onset (C3 segment) of the OAE 1a. Whether an increased value of Mo in the upper C2 indicates a short period of Mo removal into sediments under reducing conditions is uncertain, as it is not matched with an increase in other RSTE or TOC. The C4 segment is characterized by a predominance of TOC values averaging at 1.58 wt. %, indicating the periodic existence of a reducing environment that facilitated the intermittent preservation of organic matter. The segment is characterized by the predominance of dark gray, thin-bedded and finely (millimeter-scale) laminated radiolarian mudstone, wackestone and packstone with chert bands, organic-rich interbeds, and pyrite framboids (Jafarian et al., 2023). Within the C4 (excluding its basalmost part) to basalmost C5 segment there are three intervals of significant enrichment in V, Mo, and U, which are relatively well correlated with some of the highest observed values of TOC in these sediments (Fig. 6). This co-occurrence of RSTE enrichment within strata with higher TOC suggests anoxic but non-sulfidic conditions where the uptake of RSTE was mainly limited by the availability of organic substrates (Algeo and Maynard, 2004; Stein et al., 2011). The latter is also suggested by the contemporaneous enrichment in Ni and Cu, both of which occur in organic phases and may contribute to pyrite formation (Tribovillard et al., 2006). Given that pyrite framboids precipitate relatively quickly under diffusion-limited conditions and from waters at the supersaturation limit with respect to FeS or $FeS_2$ (Emmings et al., 2022), the local presence of pyrite framboids (~2–8 μm; Jafarian et al., 2023) suggests that euxinic conditions may have existed for limited periods of time within microenvironments, ambient bottom waters or porewaters. The majority of trace metals enriched in this succession can form sulfides, leading to the assumption that sulfidic (euxinic) conditions could have been present at or near the sediment-water interface in some short periods, and that reductive mobilization trapped these trace metals in the sediments (e.g., Hetzel et al., 2011; Sanchez-Hernandez and Maurrasse, 2015). That the redox conditions during the lower C4-basal C5+C6 were periodically suboxic is suggested by the intervals with decreased individual RSTE values and decreased TOC

(Fig. 6). The remaining studied succession (C5+C6) exhibits variations in TOC, where some of the higher TOC values correlate with increased Mo, albeit V and U remain low. Coupled with lithological characteristics (predominantly dark to light gray, mud-supported radiolarian and planktic foraminiferal limestone and marl), this suggests an oxic-suboxic syngenetic or early diagenetic setting for the C5+C6 segment.

Modern seawater authigenic Mo/U covariation in oxygen-depleted systems is influenced by variation in benthic redox conditions, the operation of particulate Mn-Fe-oxyhydroxide shuttle within the water column, and trace-metal chemistry of the seawater (Algeo and Tribovillard, 2009). To evaluate trace-element enrichment in ancient and modern sediments, their concentrations are expressed as enrichment factors (EF) (e.g., Calvert and Pedersen, 1993; Tribovillard et al., 2004, 2006; Brumsack, 2006; Algeo and Tribovillard, 2009). EF is simply determined by normalizing an element to Al, which is considered as a proxy for detrital influx, and relative to the AS (Wedepohl, 1971, 1991). Although both Mo and U are enriched in sediments under comparable water-column conditions, their geochemical behaviors differ significantly during the sedimentation process. The correlation between Mo-EF and U-EF can be used as a practical proxy to investigate the level of oxygen depletion relative to the Mo/U ratios in modern seawater (Algeo and Tribovillard, 2009). EFs for Mo and U in the Lower Aptian Kazhdumi Basin deposits were calculated ($EF_{element}$ = $(element/Al)_{sample}/(element/Al)_{AS}$; Wedepohl, 1971; Taylor and McLennan, 1985; Table S3). The studied Lower Dariyan Fm. is characterized by a significant enrichment in authigenic Mo (mean= 155; samples from C2, C4 and C5+C6 segments with values over 300) and U (samples fall within the range of 3 to 200), with a weak (R= +0.48) positive correlation for the entire dataset (Fig. 8). These values yield Mo/U ratios generally 0.3 to 3 times the seawater ratio, albeit most samples are considerably more enriched in Mo relative to U.

In marine sediments, the absorption of authigenic U begins at the redox boundary of Fe(II)-Fe(III) under suboxic conditions (Zheng et al., 2002). Conversely, the absorption of authigenic Mo necessitates the existence of $H_2S$ under anoxic to euxinic conditions (Zheng et al., 2000; Morford et al., 2001). Variations in sediment Mo/U ratios may occur as a result of differences in solubility attributable to redox conditions, with suboxic settings potentially yielding low Mo/U ratios and more anoxic settings potentially yielding high Mo/U ratios (Algeo and Tribovillard, 2009). The highest enrichment of U relative to Mo is recorded in the C4 sample immediately below the RFZ, which suggests a strongly restricted basinal environment in that interval. A subset of samples from the C4 segment with high TOC values exhibits the overall highest EFs with increasing Mo/U ratio around the 1x seawater molar ratio (Fig. 8). A similar pattern has previously been recorded from the deep-water OAE 1a deposits from the Subbriançonnais Basin (Charbonnier et al., 2018). Such covariation pattern is more similar to the present-day Peru Shelf, E. Tropical Pacific, than to the euxinic setting of the Black Sea, and is suggestive of greater redox variation, i.e., from suboxic to sulfidic (Algeo and Tribovillard, 2009; see their Fig. 4). A similar trend is exhibited by a subset of samples from segment C5+C6 with Mo/U ratios around the seawater value (1x SW). However, a second subset of samples from C5+C6, all samples from C3, and the majority of samples from C2 (Fig. 8; data points around and above the 3x SW line) exhibit a strong enrichment of Mo relative to U. This is suggestive of the particulate Mn-Fe oxyhydroxide shuttle, which affects Mo but does not affect the accumulation of U (e.g., Crusius et al., 1996; Algeo and Tribovillard, 2009; Tribovillard et al., 2012). It is a mechanism by which the particulate Fe-Mn oxyhydroxides that are formed at the chemocline absorb molybdate oxyanions as they settle through the water column, and are then scavenged at the seafloor thus leading to Mo enrichment relative to other RSTE in the sediment (Algeo and Tribovillard, 2009).

Finally, it is possible that, as a consequence of high-frequency changes in the redox conditions, the primary Mo/U relationships were modified by the early post-depositional remobilization of Mo and U (Algeo et al., 2004; Algeo and Tribovillard, 2009) but the extent of that is unknown. The overall shotgun-like pattern of Mo/U data clustering with only a weak trend towards higher EFs with increasing Mo/U ratios suggests highly variable redox conditions in the Kazhdumi Intrashelf Basin. Given the basin's moderately restricted setting along the NE Arabian Plate margin, the connectivity and the watermass exchange between the basin and the Neo-Tethys likely controlled the variations in benthic redox diversity.

### 5.4. Evaluation of palaeoproductivity based on trace element-TOC covariations

Copper and nickel are important micronutrients that are usually sourced from the settling organic debris but can also be absorbed into Mn-Fe oxyhydroxides (e.g., Calvert and Pedersen, 1993; Algeo and Maynard, 2004; Tribovillard et al., 2006). When sediment experiences reducing conditions, these trace metals can get incorporated into Fe sulfides or form their own sulfide phases

(Hetzel et al., 2011). Despite complete remineralization of organic matter, Ni and Cu can still be retained in sediment through sulfides (typically as a solid solution within pyrite). As a result, Cu and Ni are reliable indicators of the delivery of organic matter to the sediment (Algeo and Maynard, 2004).

Following the low Cu and Ni values recorded in C2 through basalmost C4 segments, the remaining C4 to basal C5+C6 segments are characterized by significant increases in Cu and Ni that match higher TOC values (Fig. 6), suggesting periodically increased organic matter influx. The initial increase slightly trailed the increase in phosphorus content, which triggered the increase in primary productivity (discussed below), as evidenced by the abundance of radiolarians and planktic foraminifera, particularly within the C4 to C5+C6 segments (Jafarian et al., 2023). The matching Si/Al and PSTE peaks (Cu/Al and NiAl; Fig. 6) indicate periodically high biogenic productivity from mid-C4 to basalmost C5+C6 segments, especially immediately before and during deposition of the RFZ. It is important to note that not all of the biogenic silica generated by the radiolarians was deposited because of the likely dissolution occurring in the overlying water column (Wollast and Mackenzie, 1983).

Phosphorus serves as a crucial nutrient and energy carrier across various levels of the biosphere, and periods of extensive primary productivity and terrestrial biogeochemical weathering are commonly characterized by significant increases in this element (e.g., Föllmi, 1996; Compton et al., 2000; Bodin et al., 2006). The effectiveness of phosphorus storage in a sedimentary basin relies on the redox state, and when oxygen levels are depleted, a substantial amount of phosphate can be recycled and returned into the bottom-waters (Van Cappellen and Ingall, 1994; Bodin et al., 2006; Mort et al., 2007; Beil et al., 2020). Phosphorous is transferred to the sedimentary reservoir either through its assimilation into the organic matter or by its aggregation with clay particles and Fe-Mn oxyhydroxides (Delaney, 1998).

The productivity played an important role in the development of anoxic conditions in the Kazhdumi Basin as further suggested by a strong increase in phosphorus content in the basal C4 segment that matches an increase in TOC, thus signaling an increase in nutrient availability. That this increase was not limited to this part of the Tethys is suggested by a coeval peak in TOC and phosphorus recorded in the Subbriançonnais Basin (Charbonnier et al., 2018; their Fig. 2). This correlates well with the previously suggested increase in nutrient availability that occurred in the

Kazhdumi Basin during the C3–C4 transition, as suggested by a lithological change from ostreid-dominated shallow-marine carbonates to deeper-water dark-gray limestones, chert bands, and organic-rich shales with radiolarians, sponge spicules, and planktic foraminifera (Jafarian et al., 2023). Stein et al. (2011) argued that such increased input of phosphorous into the ocean acted as a fertilizer for the southern Tethyan margin during the OAE 1a, which led to the growth of radiolarian populations, particularly in the areas with significant upwelling. Although the latter was possible, in the absence of riverine inputs and lack of evidence for extensive upwelling, it is likely that aeolian transport also played an important role in delivering terrestrial particulate phosphorus (Mackey and Paytan, 2009) into the Kazhdumi Intrashelf Basin. The decrease in phosphorus within the upper RFZ suggests that the high primary productivity was sustained by phosphorus recycling from the sediments, which in turn led to enhanced carbon burial and increased $\delta^{13}C_{carb}$ values recorded during that interval (cf., Beil et al., 2020). Several subsequent peaks in phosphorus values also correlate with smaller increases in TOC. Given the overall lack of association between lower phosphorus and higher RSTE values, it is unlikely that a significant part of phosphorus was remobilized in the bottom-waters by oxygen depletion (Charbonnier et al., 2018).

### 5.5. Causes of variations in intrashelf basin bottom water conditions during OAE 1a

The OAE 1a represents a major episode of climatic, biotic, environmental, and climatic perturbations related to a global warming event, increased marine productivity, oxygen-depleted bottom water, and increased burial of organic matter in deep-water settings (e.g., Schlanger and Jenkyns, 1976; Weissert and Bréheret, 1991; Jenkyns, 2010; Erba et al., 2015; Castro et al., 2021; Percival et al., 2021). However, its record is characterized by spatial variability in redox conditions likely related to paleogeography, freshwater input, and depth, with deeper parts of the Tethys characterized by anoxic-euxinic conditions and less reducing conditions in shallower environments (Westermann et al., 2013; Nie et al., 2023). The OAE 1a onset was characterized by a massive input of isotopically light carbon into the ocean, as evidenced by a major negative $\delta^{13}C$ excursion (Schlanger and Jenkyns, 1976; Arthur et al., 1990) in segment C3 *sensu* Menegatti et al. (1998). Climatic instability characterized the period before (C2) and the onset (C3) of the OAE 1a, and the initial pulses of volcanic activity predated the main phase (Martínez-Rodríguez et al., 2021). Also, the weathering regime was characterized by physical weathering and/or intensified erosion under drier and/or markedly seasonal rainfall (Beil et al., 2020). Intensified greenhouse conditions at the onset of the OAE 1a led to enhanced continental weathering, albeit the bottom water oxygen levels were high enough to break down the organic matter through the water column (Westermann et al., 2013). The plate-marginal position of the Kazhdumi Intrashelf Basin restricted it from significant detrital input during segments C2 through basalmost C4, as evidenced by predominantly carbonate succession with low TOC. Abundant benthic biota, especially orbitolinids and ostreid bivalves, and extensive bioturbation, coupled with low RSTE suggest oxic bottom water, and low PSTE are indicative of low productivity. The lag in nutrient increase, which in deeper intrashelf basins with predominantly marly deposits is recorded by higher phosphorus values already in C3 (e.g., Vocontian Basin; Giraud et al., 2018; Beil et al., 2020), was likely due to paleogeographic setting of the basin along the NE Arabian Plate margin and its connectivity with the Neo-Tethys Ocean.

Segment C4 is associated with a global cooling episode with upper water column temperatures dropping by ~2°C in the middle of C4, which is expressed as a positive shift in the oxygen-isotope record, and a correlative major positive shift in $\delta^{13}C$ signaling extensive deposition of organic matter (Jenkyns, 2018). The latter was enabled by the accelerated continental weathering rates (Blätter et al., 2011; Bottini et al., 2012; Lechler et al., 2015) that resulted in enhanced nutrient flux to the ocean and the associated increase in marine productivity. It is important to note that the global record of organic carbon burial documented by the positive $\delta^{13}C$ excursion is more representative for the duration of the OAE 1a than the stratigraphic extent of local black shales (Beil et al., 2020). Also, an increase in the proportion of carbonate weathering, relative to organic carbon and silicate weathering, could have maintained prolonged positive marine $\delta^{13}C$ excursions without substantially enhancing organic carbon burial (Kump and Arthur, 1999). On the Arabian Plate, the regional Early Aptian transgression (Aptian Supersequence with maximum flooding surface K80; Sharland et al., 2001; van Buchem et al., 2010) promoted input of nutrients derived from the weathered terrestrial sediments (e.g., Al-Fares et al., 1998; van Buchem et al., 2002). An increase in continental weathering was promoted by a hot and humid or seasonally wet climate (Davies et al., 2019) with an enhanced hydrological cycle. Nutrient availability boosted primary productivity and contributed to the development of the RFZ with anoxic-suboxic bottom waters during the lower C4 to basalmost C5+C6 segments, as evidenced by increased TOC and phosphorus in the Kazhdumi Basin and globally (e.g., Charbonnier et al., 2018). A significant deepening was in the basin also associated with a major biotic shift from shallow to deep open-marine biota dominated by radiolarians and planktic foraminifera. In the shallower Bab Basin further south along the plate margin as well as on the Arabian carbonate platform, the deepening was associated with the expansion of the microencrusters *Lithocodium-Bacinella* during segment C4 and continued through C6 (Immenhauser et al., 2005; Rameil et al., 2010; Yamamoto et al., 2013). The *Lithocodium-Bacinella* bloom has been associated with platform top anoxia during the OAE 1a, apparently driven either by the upwelling of oxygen-depleted basinal waters or by the development of localized oxygen minimum zones (Hueter et al., 2019). The latter is supported by localized findings of dysaerobic platy lime mudstones on the Adriatic Carbonate Platform that extend from the upper C4 to C7 (Husinec et al., 2012).

Following a significant global warming during the upper part of segment C4 and into lower C5, at least one cooling episode is globally recognized in segment C5+C6 (Jenkyns, 2018), whereas fluctuations between drier and wetter climate are locally recorded into the lower C7 (Beil et al., 2020). In the Kazhdumi Basin, this interval is characterized by a relative sea-level fall (Jafarian et al., 2023), during which the major $SiO_2$ source was biogenous silica, as suggested by low Si/Al and K/Al values (Fig. 6), and relatively high productivity was maintained by phosphorus recycling. Oscillations in TOC, RSTE, and PSTE suggest periodic changes between oxic and suboxic conditions, where the water column ventilation may have moderated TOC by organic matter destruction (cf., Nie et al., 2023). Overall, the unrelenting global productivity led to $CO_2$ drawdown, more oxic conditions, and a post-OAE 1a climate overturn towards less humid conditions (Westermann et al., 2013).

## Conclusions

A bio- and chemo-stratigraphically well-constrained succession of the Kazhdumi Intrashelf Basin exposed at Dareh Sefid, Fars Province, Iran was utilized to evaluate the trends in organic matter production, palaeoredox conditions, terrestrial input, and paleoproductivity during the OAE 1a (including carbon-isotope segments C2–C6 *sensu* Menegatti et al., 1998). The results suggest that the highly variable redox conditions in the Kazhdumi Basin during the OAE 1a were primarily controlled by the connectivity and watermass exchange with Neo-Tethys, and assisted by the nutrient input associated with continental weathering.

Carbon-isotope segments C2 through basalmost C4 are characterized by predominantly carbonate deposition with low TOC, low RSTE, and low PSTE. This, coupled with abundant orbitolinids, ostreid bivalves, and bioturbation, indicates oxic conditions prior to and at the onset (C3 segment) of the OAE 1a. The intermittently suboxic conditions are suggested by the intervals with increased RSTE or TOC. An increase in nutrient availability was marked by a significant increase in phosphorus content in the basalmost C4, which was matched by an increase in TOC.

The Kazhdumi Basin section spanning lower C4 through basalmost C5+C6 segments has several intervals with co-occurrence of high RSTE, PSTE (Cu, Ni), and TOC, indicating anoxic, albeit non-sulfidic conditions with high biogenic productivity, primarily by radiolarians and planktic foraminifera. That the surface-water productivity was driving the productivity increase is suggested by a significant decrease in $\Delta^{13}C$ values that correlates with a paired increase in $\delta^{13}C_{org}$ and $\delta^{13}C_{carb}$ in the lower RFZ. The decrease in the phosphorus content in the upper RFZ (mid-C4) suggests that the high primary productivity was also periodically sustained by phosphorus recycling from the sediments.

Segment C5+C6 (excluding its basalmost part, i.e., the top of RFZ) is part of a regressive sequence of predominantly dark gray, mud-supported radiolarian and planktic foraminiferal wackestone. The intermittently oxic-suboxic setting is indicated by variable TOC (0.2 to 2.5%), where some of the higher TOC values tie with increased molybdenum, albeit vanadium and uranium contents remain low. Both biogenous and detrital silica contributed to an increase in the $SiO_2$ content.

## Acknowledgements

This study presents the results of AJ’s Ph.D. thesis and was financially supported by the National Natural Science Foundation of China (Grant Nos. 41888101, 42072118). Funding for stable isotope analysis of organic carbon was kindly covered by the Stable Isotope Biogeochemistry Laboratory (SIBL) at Durham University. The senior author would like to thank Dr. G.C.

Gambacorta for valuable discussions. We thank editor Alex Dickson and three anonymous reviewers for their constructive comments.

## References

Adloff, M., Green, S.E., Parkinson, I.J., Naafs, B.D.A., Preston, W., Ridgwell, A., Lunt, D.J., Castro, J.M., Monteiro, F., 2020. Unravelling the sources of carbon emissions at the onset of Oceanic Anoxic Event (OAE) 1a. Earth and Planetary Science Letters 530, 1-9.

Agard, P., Omrani, J., Jolivet, L., Mouthereau, F., 2005. Convergence history across Zagros (Iran): constraints from collisional and earlier deformation. International Journal of Earth Sciences 94, 401-419.

Alavi, M., 2004. Regional stratigraphy of the Zagros fold–thrust belt of Iran and its proforeland evolution. American Journal of Science 304, 1-20.

Al-Fares, A.A., Bouman, M., Jeans, P., 1998. A new look at the Middle to Lower Cretaceous stratigraphy, offshore Kuwait. GeoArabia 3, 543-560.

Algeo, T.J., 2004. Can marine anoxic events draw down the trace-element inventory of seawater?. Geology 32, 1057-1060.

Algeo, T.J., Li, C., 2020. Redox classification and calibration of redox thresholds in sedimentary systems. Geochimica et Cosmochimica Acta 287, 8–26.

Algeo, T.J., Liu, J., 2020. A re-assessment of elemental proxies for paleoredox analysis. Chemical Geology 540, 119549.

Algeo, T.J., Maynard, J.B., 2004. Trace-element behavior and redox facies in core shales of Upper Pennsylvanian Kansas-type cyclothems. Chemical Geology 206, 289-318.

Algeo, T.J., Rowe, H., 2012. Paleoceanographic applications of trace-metal concentration data. Chemical Geology 324-325, 6-18.

Algeo, T.J., Schwark, L., Hower, J.C., 2004. High-resolution geochemistry and sequence stratigraphy of the Hushpuckney Shale (Swope Formation, eastern Kansas): implications for climato-environmental dynamics of the Late Pennsylvanian Midcontinent Seaway. Chemical Geology 206, 259-288.

Algeo, T.J., Tribovillard, N., 2009. Environmental analysis of paleoceanographic systems based on molybdenum-uranium covariation. Chemical Geology 268, 211-225.

Amodio, S., Weissert, H., 2017. Palaeoenvironment and palaeoecology before and at the onset of Oceanic Anoxic Event (OAE)1a: reconstructions from Central Tethyan archives. Palaeogeography, Palaeoclimatology, Palaeoecology 479, 71-89.

Arthur, M.A., Jenkyns, H.C., Brumsack, H.-J., Schlanger, S.O., 1990. Stratigraphy, geochemistry, and paleoceanography of organic carbon-rich Cretaceous sequences. In: Ginsburg, R.N., Beaudoin, B. (Eds.), Cretaceous Resources, Events and Rhythms: Background and Plans for Research. Kluwer, Dordrecht. NATO ASI Series 304, pp. 75-119.

Bahrehvar, M., Mehrabi, H., Rahimpour-Bonab, H., 2020. Coated grain petrography and geochemistry as palaeoenvironmental proxies for the Aptian strata of the southern Neo-Tethys Ocean, Persian Gulf, Iran. Facies 66, 3.

Bauer, K.W., Bottini, C., Frei, R., Asael, D., Planavsky, N.J., Francois, R., McKenzie, N.R., Erba, E., Crowe, S.A., 2021. Pulsed volcanism and rapid oceanic deoxygenation during Oceanic Anoxic Event 1a. Geology 49, 1452-1456.

Bauer, K.W., Bottini, C., Katsev, S., Jellinek, M., Francois, R., Erba, E., Crowe, S., 2022. Ferruginous oceans during OAE1a and collapse of the marine sulfate pool. Earth and Planetary Science Letters 578, 117324.

Bauer, K.W., Zeebe, R.E., Wortmann, U.G., 2017. Quantifying the volcanic emissions which triggered Oceanic Anoxic Event 1a and their effect on ocean acidification. Sedimentology 64, 204-214.

Beerling, D.J., Lomas, M.R., Gröcke, D.R., 2002. On the nature of methane gas-hydrate dissociation during the Toarcian and Aptian Oceanic anoxic events. American Journal of Science 302, 28-49.

Beil, S., Kuhnt, W., Holbourn, A., Scholz, F., Oxmann, J., Wallmann, K., Lorenzen, J., Aquit, M., Chellai, E.H., 2020. Cretaceous anoxic events prolonged by phosphorus cycle feedbacks. Climate of the Past 16, 757-782.

Berberian, M., King, G.C.P., 1981. Towards a paleogeography and tectonic evolution of Iran. Canadian Journal of Earth Science 18, 210-265.

Blättler, C.L., Jenkyns, H.C., Reynard, L.M., Handerson, G.M., 2011. Significant increases in global weathering during Oceanic Anoxic Events 1a and 2 indicated by calcium isotopes. Earth and Planetary Science Letters 309, 77-88.

Blok, C.N., Ineson, J., Anderskouv, K., Fantasia, A., Sheldon, E., Thibault, N., Jelby, M.E., Adatte, T., Bodin, S., 2022. Latitude-dependant climate changes across the Aptian Oceanic Anoxic Event 1a. Palaeogeography, Palaeoclimatology, Palaeoecology 601, 111085.

Bodin S., Godet A., Föllmi K.B., Vermeulen J., Arnaud H., Strasser A., Fiet, N., Adatte T., 2006. The late Hauterivian Faraoni oceanic anoxic event in the western Tethys: evidence from phosphorus burial rates. Palaeogeography, Palaeoclimatology, Palaeoecology 235, 245-264.

Boning, P., Brumsack, H.J., Bottcher, M.E., Schnetger, B., Kriete, C., Kallmeyer, J., Borchers, S.L., 2004. Geochemistry of Peruvian near-surface sediments. Geochimica et Cosmochimica Acta 68, 4429-4451.

Bordenave, M.L., Burwood, R., 1989. Source rock distribution and maturation in the Zagros orogenic belt: provenances of the Asmari and Bangestan reservoir oil accumulation. Organic Geochemistry 16, 369-387.

Bordenave, M.L., Hegre, J.A., 2005. The influence of tectonics on the entrapment of oil in the Dezful embayment, Zagros fold belt, Iran. Journal of Petroleum Geology 28, 339-368.

Bordenave, M.L., Hegre, J.A., 2010. Current distribution of oil and gas fields in the Zagros Fold Belt of Iran and contiguous offshore as the result of the petroleum systems. Geological Society of America Special Publication 330, 291-353.

Bottini, C., Cohen, A.S., Erba, E., Jenkyns, H.C., Coe, A.L., 2012. Osmium-isotope evidence for volcanism, weathering and ocean mixing during the early Aptian OAE 1a. Geology 40, 583-586.

Bover-Arnal, T., Salas, R., Guimera, J., Moreno-Bedmar, J.A., 2022. Eustasy in the Aptian world: a vision from the eastern margin of the Iberian Plate. Global and Planetary Change 214, 103849.

Brand, U., Veizer, J., 1980. Chemical diagenesis of a multicomponent carbonate system 1. Trace elements. Journal of Sedimentary Petrology 50, 1219-1236.

Brumsack, H.J., 1989. Geochemistry of recent TOC-rich sediments from the Gulf of California and the Black Sea. Geologische Rundschau 78, 851-882.

Brumsack, H.J., 2006. The trace metal content of recent organic carbon-rich sediments: implications for Cretaceous black shale formation. Palaeogeography, Palaeoclimatology, Palaeoecology 232, 344-361.

Calvert, S.E., Pedersen, T.F., 1993. Geochemistry of recent oxic and anoxic marine sediment: implications for the geological record. Marine Geology 113, 67-88.

Castro, J.M., Ruiz-Ortiz, P.A., de Gea, G.A., Aguado, R., Jarvis, I., Weissert, H., Molina, J.M., Nieto, L.M., Pancost, R.D., Quijano, M.L., Reolid, M., Skelton, P.W., López-Rodríguez, C., Martínez-Rodríguez, R., 2021. High-resolution C-isotope, TOC and biostratigraphic records of OAE 1a (Aptian) from an expanded hemipelagic cored succession, western Tethys: a new stratigraphic reference for global correlation and paleoenvironmental reconstruction. Paleoceanography and Paleoclimatology 36, e2020PA004004.

Charbonnier, G., Adatte, T., Spangenberg, J.E., Föllmi, K.B., 2018. The expression of early Aptian to latest Cenomanian oceanic anoxic events in the sedimentary record of the Briançonnais domain. Global and Planetary Change 170, 76-92.

Charbonnier, G., Föllmi, K.B., 2017. Mercury enrichments in lower Aptian sediments support the link between Ontong Java large igneous province activity and oceanic anoxic episode 1a. Geology 45, 63-66.

Compton, J., Mallinson, D., Glenn, C., Filippelli, G., Föllmi, K., Shields, G., Zanin, Y., 2000. Variations in the global phosphorus cycle. In: Glenn, C., Prévôt-Lucas, L., Lucas, J. (Eds.), Marine Authigenesis: From Microbial to Global. SEPM Special Publications 66, pp. 21-34.

Crusius, J., Calvert, S., Pedersen, T., Sage, D., 1996. Rhenium and molybdenum enrichments in sediments as indicators of oxic, suboxic and sulfidic conditions of deposition. Earth and Planetary Science Letters 145, 65.

Davies, R.B., Simmons, M.D., Jewell, T.O., Collins, J., 2019. Regional Controls on Siliciclastic Input into Mesozoic Depositional Systems of the Arabian Plate and Their Petroleum Significance. In: AlAnzi, H.R., Rahmani, R.A., Steel, R.J., Soliman, O.M. (Eds.), Siliciclastic reservoirs of the Arabian Plate. AAPG Memoir 116, pp. 103-140.

Delaney, M.L., 1998. Phosphorus accumulation in marine sediments and the oceanic phosphorus cycle. Global Biogeochemical Cycles 12, 563-572.

Dellwig, O., Hinrichs, J., Hild, A., Brumsack, H.J., 2000. Changing sedimentation in tidal flat sediments of the southern North Sea from the Holocene to the present: a geochemical approach. Journal of Sea Research 44, 163-181.

Edwards, C.T., Saltzman, M.R., 2016. Paired carbon isotopic analysis of Ordovician bulk carbonate ($\delta^{13}C_{carb}$) and organic matter ($\delta^{13}C_{org}$) spanning the Great Ordovician Biodiversification Event. Palaeogeography, Palaeoclimatology, Palaeoecology 458, 102-117.

Emmings, J.F., Poulton, S.W., Walsh, J., Leeming, K.A., Ross, I., Peters, S.E., 2022. Pyrite mega-analysis reveals modes of anoxia through geological time. Science Advances 8, eabj5687.

Erba, E., 2004. Calcareous nannofossils and Mesozoic oceanic anoxic events. Marine Micropaleontology 52, 85-106.

Erba, E., Duncan, R.A., Bottini, C., Tiraboschi, D., Weissert, H., Jenkyns, H.C., Malinverno, A., 2015. Environmental consequences of Ontong Java Plateau and Kerguelen Plateau volcanism. In: Neal, C.R., Sager, W.W., Sano. T., Erba, E. (Eds.), The Origin, Evolution, and Environmental Impact of Oceanic Large Igneous Provinces. Geological Society of America Special Paper 511, pp. 271-303.

Fakhari, M.D., Axen, G.J., Horton, B.K., Hassanzadeh, J., Amini, A., 2008. Revised age of proximal deposits in the Zagros foreland basin and implications for Cenozoic evolution of the High Zagros. Tectonophysics 451, 170-185.

Falcon, N.L., 1958. Position of oil fields of southwest Iran with respect to relevant sedimentary basins. In: Weeks, L.G. (Ed.), Habitat of Oil. Tulsa, Oklahoma, pp. 1279-1293.

Fantle, M.S., Barnes, B.D., Lau, K.V., 2020. The Role of Diagenesis in Shaping the Geochemistry of the Marine Carbonate Record. Annual Review of Earth and Planetary Sciences 48, 549-583.

Föllmi, K.B., 1996. The phosphorus cycle, phosphogenesis and marine phosphate-rich deposits. Earth Science Reviews 40, 55-124.

Föllmi, K.B., 2012. Early Cretaceous life and anoxia. Cretaceous Research 35, 230-257.

Gambacorta, G., C. Bottinia, C., Brumsackb, H.-J., Schnetgerb, B., Erba, E., 2020. Major and trace element characterization of Oceanic Anoxic Event 1d (OAE 1d): insight from the Umbria-Marche Basin, central Italy. Chemical Geology 229, 104022.

Gibbs, S.J., Robinson, S.A., Brown, P.R., Dunkley Jones, T., Henderiks, J., 2011. Comment on "Calcareous Nannoplankton Response to Surface-Water Acidification Around Oceanic Anoxic Event 1a". Science 332, 175.

Giraud, F., Pittet, B., Grosheny, D., Baudin, F., Lécuyer, C., Sakamoto, Y., 2018. The palaeoceanographic crisis of the Early Aptian (OAE 1a) in the Vocontian Basin (SE France). Palaeogeography, Palaeoclimatology, Palaeoecology 511, 483-505.

Golonka, J., 2000. Cambrian–Neogen Plate Tectonic Maps. Wydawnictwo Uniwersytetu Jagiellońskiego, Kraków, Poland, 125 p.

Granier, B., Clavel, B., Moullade, M., Busnardo, R., Charollais, J., Tronchetti, G., Desjacques, P., 2017. L'Estellon (Baronnies, France), a "Rosetta Stone" for the Urgonian biostratigraphy. In: Granier, B. (Ed.), Some Key Lower Cretaceous sites in Drôme (SE France), Carnets de Géologie, Association Carnets de Géologie, Brest, CG2017_B01, pp. 111-158.

Graziano, R., Raspini, A., Bartiromo, A., 2016. Late Aptian palaeoclimatic turnovers and volcanism: Insights from a shallow-marine and continental succession of the Apennine carbonate platform, southern Italy. Sedimentary Geology 339, 188-217.

Gröcke, D.R., Hesselbo, S.P., Jenkyns, H.C., 1999. Carbon-isotope composition of Lower Cretaceous fossil wood: ocean-atmosphere chemistry and relation to sea-level change. Geology 27, 155-158.

Gröcke, D.R., 2002. The carbon isotope composition of ancient $CO_2$ based on higher-plant organic matter. Philosophical Transactions of the Royal Society Series A 360, 633-658.

Hatch, J. R., Jacobson, S. R.,Witzke, B. J., Risatti, J. B., Anders, D. E.,Watney,W. L., Newell, K. D., Vuletich, A. K., 1987, Possible late Middle Ordovician carbon isotope excursion: Evidence from Ordovician oils and hydrocarbon source rocks, Mid-Continent and east-central United States. AAPG Bulletin 71, 1342-1354.

Hayes, J.M., Strauss, H., Kaufman, A.J., 1999. The abundance of $^{13}C$ in marine organic matter and isotopic fractionation in the global biogeochemical cycle of carbon during the past 800 Ma. Chemical Geology 161, 103-125.

Hetzel, A., März, C., Vogt, C., Brumsack, H.J., 2011. Geochemical environment of Cenomanian-Turonian black shale deposition at Wunstorf (northern Germany). Cretaceous Research 32, 480-494.

Heydari, E., 2008. Tectonic versus eustatic control on supersequences of the Zagros Mountains of Iran. Tectonophysics 451, 56-70.

Horton, B.K., Hassanzadeh, J., Stockli, D.F., Axen, G.H., Gillis, R.J., Guest, B., Amini, A., Fakhari, M., Zamanzadeh, S.M., Grove, M., 2008. Detrital zircon provenance of Neoproterozoic to Cenozoic deposits in Iran: implications for chronostratigraphy and collisional tectonics. Tectonophysics 451, 97-122.

Huck, S., Rameil, N., Korbar, T., Heimhofer, U., Wieczorek, T.D., Immenhauser, A., 2010. Latitudinally different responses of Tethyan shoal-water carbonate systems to the Early Aptian oceanic anoxic event (OAE 1a). Sedimentology 57, 1585-1614.

Hueter, A., Huck, S., Bodin, S., Heimhofer, U., Weyer, S., Jochum, K.P., Immenhauser, I., 2019. Central Tethyan platform-top hypoxia during Oceanic Anoxic Event 1a. Climates of the Past 15, 1327-1344.

Husinec, A., 2001. *Palorbitolina lenticularis* from the northern Adriatic region: palaeogeographical and evolutionary implications. Journal of Foraminiferal Research 31, 287-293.

Husinec, A., Harman, C.A., Regan, S.P., Mosher, D.A., Sweeney, R.J., Read, J.F., 2012. Sequence development influenced by intermittent cooling events in the Cretaceous Aptian greenhouse, Adriatic platform, Croatia. AAPG Bulletin 96, 2215-2244.

Husinec, A., Jelaska, V., 2006. Relative sea-level changes recorded on an isolated carbonate platform: Tithonian to Cenomanian succession, southern Croatia. Journal of Sedimentary Research 76, 1120-1136.

Husinec, A., Read, J.F., 2018. Cyclostratigraphic and $d^{13}C$ record of the Lower Cretaceous Adriatic Platform, Croatia: assessment of Milankovitch-forcing. Sedimentary Geology 373, 11-31.

Husinec, A., Sokač, B., 2006. Early Cretaceous benthic associations (foraminifera and calcareous algae) of a shallow tropical-water platform environment (Mljet Island, southern Croatia). Cretaceous Research 27, 418-441.

Immenhauser, A., Hillgärtner, H., Van Bentum, E., 2005. Microbial-foraminiferal episodes in the Early Aptian of the southern Tethyan margin: ecological significance and possible relation to Oceanic Anoxic Event 1a. Sedimentology 52, 77-99.

Jafarian, A., Husinec, A., Wang, C., Chen, X., Saboor, A., Li, Y., 2023. Aptian oceanic anoxic event 1a in the shallow, carbonate-dominated intrashelf Kazhdumi Basin, Zagros Mountains. Sedimentology 70, 1981-2014.

James, G.A., Wynd, J.G., 1965. Stratigraphic nomenclature of Iranian oil consortium agreement area. AAPG Bulletin 49, 2182-2245.

Jenkyns, H.C., 2010. Geochemistry of Oceanic Anoxic Events. Geochemistry, Geophysics, Geosystems 11, Q03004.

Jenkyns, H.C., 2018. Transient cooling episodes during Cretaceous Oceanic Anoxic Events with special reference to OAE 1a (Early Aptian). Philosophical Transactions of the Royal Society of London 376, 20170073.

Karakitsios, V., 1995. The influence of preexisting structure and halokinesis on organic matter preservation and thrust system evolution in the Ionian basin, northwestern Greece. AAPG Bulletin 79, 960-980.

Koinig, K.A., Shotyk, W., Lotter, A.F., Ohlendorf, C., Sturm, M., 2003. 9000 years of geochemical evolution of lithogenic major and trace elements in the sediment of an alpine lake–the role of climate, vegetation, and land-use history. Journal of Paleolimnology 30, 307-320.

Koop, W.J., Stoneley, R., 1982. Subsidence history of the Middle East Zagros Basin, Permian to Recent. Philosophical Transactions of the Royal Society of London 305, 149-168.

Kump, L.R., Arthur, M.A., 1999. Interpreting carbon-isotope excursions: carbonates and organic matter. Chemical Geology 161, 181-198.

Lechler, M., von Strandmann, P., Jenkyns, H.C., Prosser, G., Parente, M., 2015, Lithium-isotope evidence for enhanced silicate weathering during OAE 1a (Early Aptian Selli event). Earth and Planetary Science Letters 432, 210-222.

Li, Y.X., Bralower, T.J., Montañez, I.P., Osleger, D.A., Arthur, M.A., Bice, D.M., Herbert, T.D., Erba, E., Premoli Silva, I., 2008. Toward an orbital chronology for the Early Oceanic Anoxic Event (OAE1a, ~120 Ma). Earth and Planetary Science Letters 271, 88-100.

Lini, A., Weissert, H., Erba, E., 1992. The Valanginian carbon isotope event: a first episode of greenhouse climate during the Cretaceous. Terra Nova 4, 374-384.

Mackey, K.R.M., Paytan, A., 2009. Phosphorus cycle. In: Schaechter, M. (Ed.), Encyclopedia of Microbiology (Third Edition). Mackey Academic Press, pp. 322-334.

Martínez-Rodríguez, R., Selby, D., Castro, J.M., de Gea, G.A., Nieto, L.M., Ruiz-Ortiz, P.A., 2021. Tracking magmatism and oceanic change through the early Aptian Anoxic Event (OAE 1a) to the late Aptian: insights from osmium isotopes from the westernmost Tethys (SE Spain) Cau Core. Global and Planetary Change 207, 103652.

Masse, J.P., Bellion, Y., Benkhelil, J., Ricou, L.-E., Dercourt, J., Guiraud, R., 1993. Early Aptian (114 to 111 Ma). In: Dercourt, J., Ricou, L.E., Vrielynck, B. (Eds.), Atlas Tethys Palaeoenvironmental Maps: Explanatory Notes. Gauthier-Villars, Paris, pp. 135-152.

Matsumoto, H., Coccioni, R., Frontalini, F., Shirai, K., Jovane, L., Trindade, R., Savian, J. F., Kuroda, J., 2022. Mid-cretaceous marine Os isotope evidence for heterogeneous cause of oceanic anoxic events. Nature Communications 13, 239.

Matthews, R.K., Frohlich, C., 2002. Maximum flooding surfaces and sequence boundaries: comparisons between observations and orbital forcing in the Cretaceous and Jurassic (65-190 Ma). GeoArabia 7, 503-538.

Mehrabi, H., Rahimpour-Bonab, H., 2014. Paleoclimate and tectonic controls on the depositional and diagenetic history of the Cenomanian–early Turonian carbonate reservoirs, Dezful Embayment, SW Iran. Facies 60, 147-167.

Mehrabi, H., Rahimpour-Bonab, H., 2018. Palaeo-exposure surfaces in the Aptian Dariyan Formation, Offshore SW Iran: geochemistry and reservoir implications. Journal of Petroleum Geology 41, 467–494.

Mehrabi, H., Rahimpour-Bonab, H., Hajikazemi, E., Esrafili-Dizaji, B., 2015. Geological reservoir characterization of the Lower Cretaceous Dariyan Formation (Shu'aiba equivalent) in the Persian Gulf, southern Iran. Marine and Petroleum Geology 68, 132–157.

Menegatti, A.P., Weissert, H., Brown, R.S., Tyson, R.V., Farrimoud, P., Strasser, A., Caron, M., 1998. High-resolution δ13C stratigraphy through the early Aptian “Livello Selli” of the Alpine Tethys. Paleoceanography 13, 530-545.

Morford, J.L., Russell, A.D., Emerson, S., 2001. Trace metal evidence for changes in the redox environment associated with the transition from terrigenous clay to diatomaceous sediment, Saanich Inlet, BC. Marine Geology 174, 355-369.

Mort, H.P., Adatte, T., Föllmi, K.B., Keller, G., Steinmann, P., Matera, V., Berner, Z., Stüben, D., 2007. Phosphorus and the roles of productivity and nutrient recycling during oceanic anoxic event 2. Geology 35, 483-486.

Murris, R.J. 1980. Middle East: Stratigraphic evolution and Oil habitat. AAPG Bulletin, 64, 597-618.

Mutterlose, J., Bottini, C., Schouten, S., Sinninghe Damsté, J.S., 2014. High sea-surface temperatures during the early Aptian Oceanic Anoxic Event 1a in the Boreal Realm. Geology 42, 439-442.

Nie, Y., Fu, X., Wei, H., Lin, F., Zeng, S., Mansour, A., Zhou, G., Wang, W., 2023. Paleoenvironmental reconstruction preceding and during the early Aptian Oceanic Anoxic Event 1a in southern Tibet, eastern Tethys. Cretaceous Research 150, 105604.

Oehlert, A.M., Swart, P.K., 2014. Interpreting carbonate and organic carbon isotope covariance in the sedimentary record. Nature Communications 5, 4672.

Patzkowsky, M.E., Slupik, L.M., Arthur, M.A., Pancost, R.D., Freeman, K.H., 1997. Late Middle Ordovician environmental change and extinction: Harbinger of the Late Ordovician or continuation of Cambrian patterns?. Geology 25, 911-914.

Percival, L.M.E., Tedeschi, L.R., Creaser, R.A., Bottini, C., Erba, E., Giraud, F., Svensen, H., Savian, J., Trindade, R., Coccioni, R., Frontalini, F., Jovane, L., Mather, T.A., Jenkyns, H.C., 2021. Determining the style and provenance of magmatic activity during the Early Aptian Oceanic Anoxic Event (OAE 1a). Global and Planetary Change 200, 103461.

Peybernès, B., 1982. Les Orbitolinidés crétacés d'Afrique: essai de synthèse. Cahiers de Micropaléontologie 2, 13-28.

Pierson, B.J., Eberli, G.P., Al-Mehsin, K., Al-Menhali, S., Warrlich, G., Droste, H.J., Maurer, F., Whitworth, J., Drysdale, D., 2010. Seismic stratigraphy and depositional history of the Upper Shu'aiba (Late Aptian) in the UAE and Oman. In: van Buchem, F.S.P., Al-Husseini, M.I., Maurer, F., Droste, H.J. (Eds), Barremian-Aptian Stratigraphy and Hydrocarbon Habitat of the Eastern Arabian Plate. GeoArabia Special Publication 4, pp. 411-444.

Piryaei, A., Reijmer, J.J.G., van Buchem, F.S.P., Yazdi-Moghadam, M., Sadouni, J., Danelian, T., 2010. The influence of Late Cretaceous tectonic processes on sedimentation patterns along the northeastern Arabian plate margin (Fars Province, SW Iran). Geological Society, London, Special Publication 330, 211-251.

Popp, B.N., Laws, E.A., Bidigare, R.R., Dore, J.E., Hanson, K.L., Wakeham, S.G., 1998. Effect of phytoplankton cell geometry on carbon isotopic fractionation. Geochimica et Cosmochimica Acta 62, 69-77.

Rameil, N., Immenhauser, A., Warrlich, G.M.D., Hillgärtner, H., Droste, H.J., 2010. Morphological patterns of Aptian *Lithocodium–Bacinella* geobodies – relation to environment and scale. Sedimentology 57, 883–911.

Razin, P., Taati, F., van Buchem, F.S.P., 2010. Sequence stratigraphy of Cenomanian–Turonian carbonate platform margins (Sarvak Formation) in the high Zagros, SW Iran: an outcrop reference model for the Arabian plate. In: van Buchem, F.S.P., Gerdes, K.D., Esteban, M. (Eds.), Mesozoic and Cenozoic Carbonate Systems of the Mediterranean and the Middle East: Stratigraphic and Diagenetic Reference Models. Geological Society of London Special Publication 329, pp. 1-7.

Rimmer, S.M., 2004. Geochemical paleoredox indicators in Devonian–Mississippian black shales, central Appalachian Basin (U.S.A.). Chemical Geology 206, 373-391.

Sames, B., Wagreich, M., Conrad, C.P., Iqbal, S., 2020. Aquifer-eustasy as the main driver of short-term sea-level fluctuations during Cretaceous hothouse climate phases. In: Wagreich, M., Hart, M.B., Sames, B., Yilmaz, I.O. (Eds.), Cretaceous Climate Events and Short-Term Sea-Level Changes. Geological Society of London Special Publication 498, pp. 9-38.

Sanchez-Hernandez, Y., Maurrasse, F.J.-M.M., 2015. The influence of regional factors in the expression of oceanic anoxic event 1a (OAE1a) in the semi-restricted Organyà Basin, south-central Pyrenees, Spain. Palaeogeography, Palaeoclimatology, Palaeoecology 441, 582-598.

Schlagintweit, F., Rashidi, K., 2022. *Neorbitolinopsis conica* (Matsumaru in Matsumaru and Furusawa, 2007) comb. nov., a Lower Cretaceous marker from the *Orbitolina* Limestone of Central Iran. Revue de Micropaléontologie 75, 100680.

Schlanger, S.O., Jenkyns, H.C., 1976. Cretaceous oceanic anoxic events: causes and consequences. Geol. Mijnbouw, 55, 179-184.

Schroeder, R., van Buchem, F., Cherchi, A., Baghbani, D., Vincent, B., Immenhauser, A., Granier, B., 2010. Revised orbitolinid biostratigraphic zonation for the Barremian-Aptian of the eastern Arabian Plate and implications for regional stratigraphic correlations. GeoArabia Special Publication 4, 49-96.

Scott, C., Lyons, T.W., 2012. Contrasting molybdenum cycling and isotopic properties in euxinic versus non-euxinic sediments and sedimentary rocks: refining the paleoproxies. Chemical Geology 324-325, 19-27.

Sharland, P.R., Archer, R., Casey, D.M., Davies, R.B., Hall, S.H., Heward, A.P., Horbury, A.D., Simmons, M.D., 2001. Arabian Plate sequence stratigraphy. GeoArabia 2, 371.

Simmons, M.D., Miller, K.G., Ray, D.C., Davies, A., van Buchem, F.S.P., Gréselle, B., 2020. Phanerozoic Eustasy. In: Gradstein, F.M., Ogg, J.G., Schmitz, M.D., Ogg, G.M. (Eds.), Geologic Time Scale 2020, volume 1. Elsevier, pp. 357-400.

Sluijs, A., Dickens, G.R., 2012. Assessing offsets between the $\delta^{13}C$ of sedimentary components and the global exogenic carbon pool across early Paleogene carbon cycle perturbations. Global Biogeochemical Cycles 26, 1-14.

Smith, A.G., Smith, D.G., Funnell, B.M., 1994. Atlas of Mesozoic and Cenozoic coastlines. Cambridge University Press, Cambridge.

Stein, M., Föllmi, K. B., Westermann, S., Godet, A., Adatte, T., Matera, V., Fleitmann, D., Berner, Z., 2011. Progressive palaeoenvironmental change during the late Barremian–early Aptian as prelude to Oceanic Anoxic Event 1a: evidence from the Gorgo a Cerbara section (Umbria-Marche basin, central Italy). Palaeogeography and Palaeoclimatology 302, 396-406.

Steuber, T., Alsuwaidi, M., Hennhoefer, D., Sulieman, H., AlBlooshi, A., McAlpin, T.D., Shebl, H., 2022. Environmental change and carbon-cycle dynamics during the onset of Cretaceous oceanic anoxic event 1a from a carbonate-ramp depositional system, Abu Dhabi, U.A.E. Palaeogeography, Palaeoclimatology, Palaeoecology 601, 111086.

Steuber, T., Rauch, M., Masse, J.-P., Graaf, J., Malkoc, M., 2005. Low-latitude seasonality of Cretaceous temperatures in warm and cold episodes. Nature 437, 1341-1344.

Stöcklin, J., 1968. Structural history and tectonics of Iran: a review. AAPG Bulletin 52, 1229-1258.

Swart, P.K., Kennedy, M.J., 2012. Does the global stratigraphic reproducibility of $\delta^{13}C$ in Neoproterozoic carbonates require a marine origin? a Pliocene–Pleistocene comparison. Geology 40, 87-90.

Tarduno, J.A., Sliter, W.V., Kroenke, L., Leckie, M., Mater, H., Mahoney, J.J., Musgrave, R., Storey, M., Winterer, E.L., 1991. Rapid Formation of Ontong Java Plateau by Aptian Mantle Plume Volcanism. Science 254, 399-403.

Taylor, R.S., McLennan, S.M., 1985. The Continental Crust: Its Composition and Evolution. Blackwell, Oxford.

Tejada, M.L.G., Suzuki, K., Kuroda, J., Coccioni, R., Mahoney, J.J., Ohkouchi, N., Sakamoto, T., Tatsumi, Y., 2009. Ontong Java Plateau eruption as a trigger for the Early Aptian oceanic anoxic event. Geology 37, 855-858.

Tribovillard, N., Algeo, T.J., Baudin, F., Riboulleau, A., 2012. Analysis of marine environmental conditions based on molybdenum–uranium covariation–applications to Mesozoic paleoceanography. Chemical Geology 324-325, 46-58.

Tribovillard, N., Algeo, T.J., Lyons, T., Riboulleau, A., 2006. Trace metals as paleoredox and paleoproductivity proxies: an update. Chemical Geology 232, 12-32.

Tribovillard, N., Riboulleau, A., Lyons, T., Baudin, F., 2004. Enhanced trapping of molybdenum by sulfurized marine organic matter of marine origin in Mesozoic limestones and shales. Chemical Geology 213, 385-401.

van Buchem, F.S.P., Baghbani, D., Bulot, L.G., Caron, M., Gaumet, F., Hosseini, S.A., Keyvani, F., Schroeder, R., Swennen, R., Vedrenne, V., Vincent, B., 2010. Barremian–Lower Albian sequence stratigraphy of southwest Iran (Gadvan, Dariyan and Kazhdumi formations) and its comparison with Oman, Qatar and the United Arab Emirates. GeoArabia Special Publication 4, 503-548.

van Buchem, F.S.P., Pittet, B., Hillgärtner, H., Grötsch, J., Al Mansouri, A.I., Billing, I.M., Droste, H.H.J., Oterdoom, W.H., van Steenwinkel, M., 2002. High-resolution Sequence Stratigraphic Architecture of Barremian/Aptian Carbonate Systems in Northern Oman and the United Arab Emirates (Kharaib and Shu’aiba Formations). GeoArabia 7, 461-500.

Van Cappellen, P., Ingall, E.D., 1994. Benthic phosphorus regeneration, net primary production, and ocean anoxia: a model of the coupled marine biogeochemical cycles of carbon and phosphorus. Paleoceanography 9, 677-692.

Van der Weijden, C.H., 2002. Pitfalls of normalization of marine geochemical data using a common divisor. Marine Geology 184, 167-187.

Vincent, B., van Buchem, F.S.P., Bulot, L.G., Immenhauser, A., Caron, M., Baghbani, D., Huc, A.Y., 2010. Carbon-isotope stratigraphy, biostratigraphy and organic matter distribution in the Aptian–Lower Albian successions of southwest Iran (Dariyan and Kazhdumi formations). GeoArabia 4, 139-197.

Wedepohl, K.H., 1971. Environmental influences on the chemical composition of shales and clays. In: Ahrens, L.H., Press, F., Runcorn, S.K., Urey, H.C. (Eds.), Physics and Chemistry of the Earth, 8. Pergamon, Oxford, 305-333.

Wedepohl, K.H., 1991. The composition of the upper earth's crust and the natural cycles of selected metals. Metals in natural raw materials. Natural Resources. In: Merian, E. (Ed.), Metals and Their Compounds in the Environment. Weinheim, VCH, pp. 3-17.

Weissert, H., Bréheret, J.G., 1991. A carbonate-isotope record from Aptian-Albian sediments of the Vocontian Troght (SE France). Bulletin de la Société géologique de France 162, 1133–1140.

Weissert, H., Lini, A., F¨ollmi, K.B., Kuhn, O., 1998. Correlation of early cretaceous carbon isotope stratigraphy and platform drowning events: a possible link?. Palaeogeography, Palaeoclimatology, Palaeoecology 137, 189-203.

Westermann, S., Stein, M., Matera, V., Fiet, N., Fleitmann, D., Adatte, T., Föllmi, K.B., 2013. Rapid changes in the redox conditions of the western Tethys Ocean during the early Aptian Oceanic Anoxic Event. Geochimica et Cosmochimica Acta 121, 467–486.

Wignall, P.B., Twitchett, R.J., 1996. Oceanic anoxia and the end Permian mass extinction. Science 272, 1155-1158.

Wohlwend, S., Hart, M., Weissert, H., 2016. Chemostratigraphy of the Upper Albian to Mid-Turonian Natih Formation (Oman)–how authigenic carbonate changes a global pattern. The Depositional Record 2, 97-117.

Wollast, R., Mackenzie, F.T., 1983. The global cycle of silica. In: Aston, S.R. (Ed.), Silicon Geochemistry and Biogeochemistry. Academic Press, London, pp. 39-76.

Wrobel-Daveau, J.C., Ringenbach, J.C., Tavakoli, S., Ruiz, G.M.H., Masse, P., Frizon de Lamotte, D., 2010. Evidence for mantle exhumation along the Arabian margin in the Zagros (Kermanshah area, Iran). Arabian Journal of Geoscience 3, 499-513.

Yamamoto, K., Ishibashi, M., Takayanagi, H., Asahara, Y., Sato, T., Nishi, H., Iryu, Y., 2013. Early Aptian paleoenvironmental evolution of the Bab Basin at the southern Neo-Tethys margin: response to global carbon-cycle perturbations across Ocean Anoxic Event 1a. Geochemistry, Geophysics, Geosystems 14, 1104-1130.

Yavari, M., Yazdi, M., Ghalavand, H., Adabi, M.H., 2017. Urgonian type microfossils of the Dariyan Formation, from Southwest of Iran (northeast of Shiraz). Journal of Sciences (Iran) 28, 255-265.

Yose, L.A., Ruf, A.S., Strohmenger, C.J., Al-Hosani, I., Al-Maskary, S., Bloch, G., Al-Mehairi, Y., Schuelke, J.S., Gombos, A., Johnson, I.G., 2006. Three-dimensional characterization of a heterogeneous carbonate reservoir, Lower Cretaceous, Abu Dhabi (United Arab Emirates). In: Harris, P.M., Weber, L.J. (Eds.), Giant hydrocarbon reservoirs of the world: From rocks to reservoir characterization and modeling. AAPG Memoir 88, pp. 173–212.

Zheng, Y., Anderson, R.F., van Geen, A., Fleisheir, M.Q., 2002. Remobilization of authigenic uranium in marine sediments by bioturbation. Geochemica et Cosmochimica Acta 66, 1759-1772.

Zheng, Y., Anderson, R.F., van Geen, A., Kuwabara, J., 2000. Authigenic molybdenum formation in marine sediments: a link to pore water sulfide in the Santa Barbara Basin. Geochemica et Cosmochimica Acta 64, 4165-4178.

## Figure and Table captions

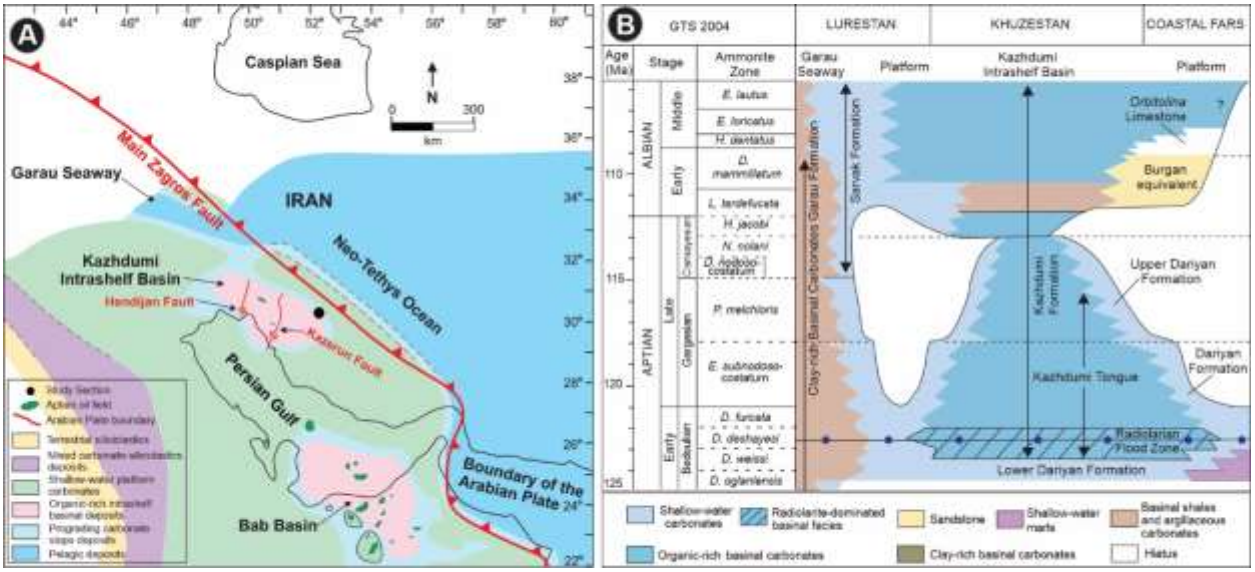

**Fig. 1.** (A) Palaeogeographical map of the Arabian Plate during the Aptian (van Buchem et al., 2010). (B) Generalized chronostratigraphy, biostratigraphy, and lithostratigraphy chart of the Barremian–Lower Albian of the Zagros Mountains, Iran (van Buchem et al., 2010).

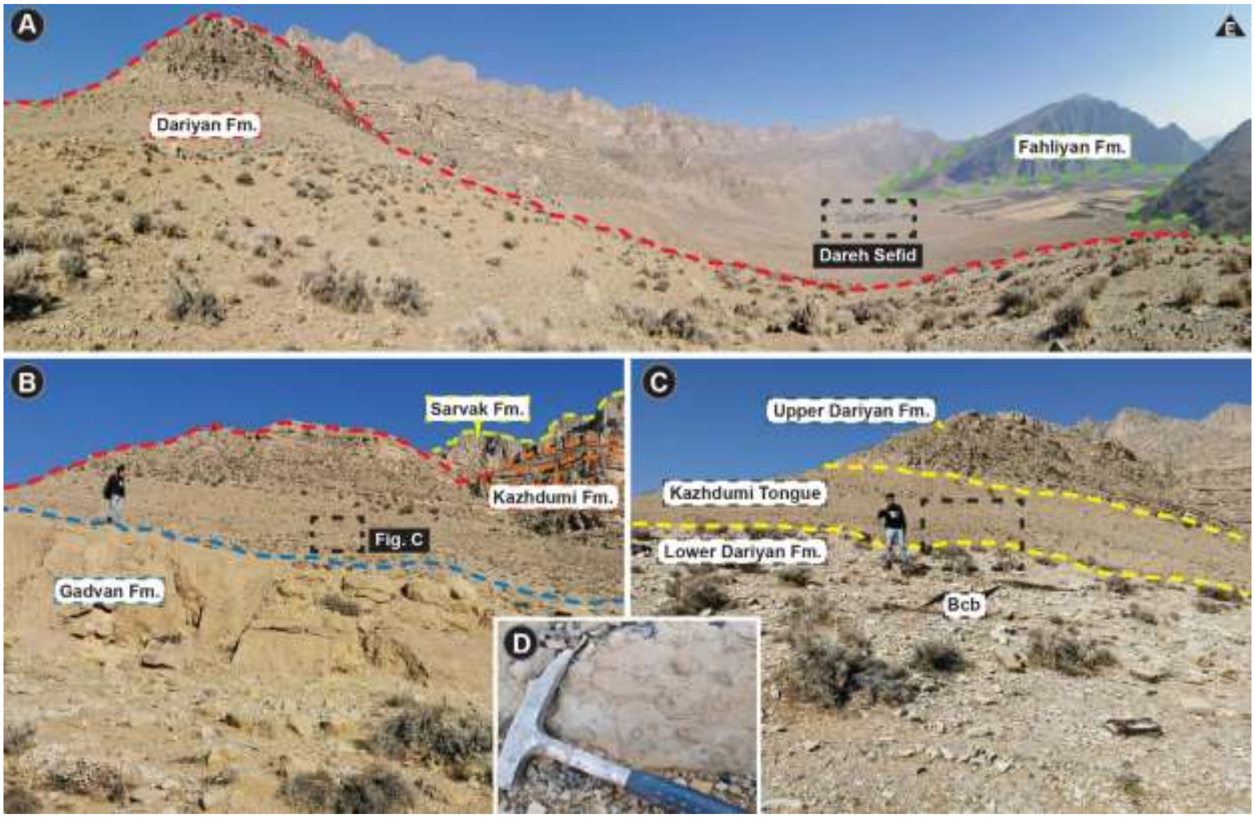

**Fig. 2.** Outcrop photographs of the Aptian Dariyan Formation at the Dareh Sefid section. (A) Panoramic view shows the location of the Dareh Sefid village relative to the hillside exposures of the Dariyan Fm. (B) Closer view of the conformable contacts between the Dariyan and Gadvan Fms. and between the Sarvak and the Kazhdumi Fms. on top of the Dariyan Formation. (C) Close-up view of the Lower Dariyan contact with Kazhdumi Tongue. Note the color and lithology change at the contact between Lower Dariyan unit (light gray thin-bedded limestones with frequent black chert bands (Bcb)) and Kazhdumi Tongue (middle unit; greenish gray shales). (D) Shelly limestone bed, Lower Dariyan unit.

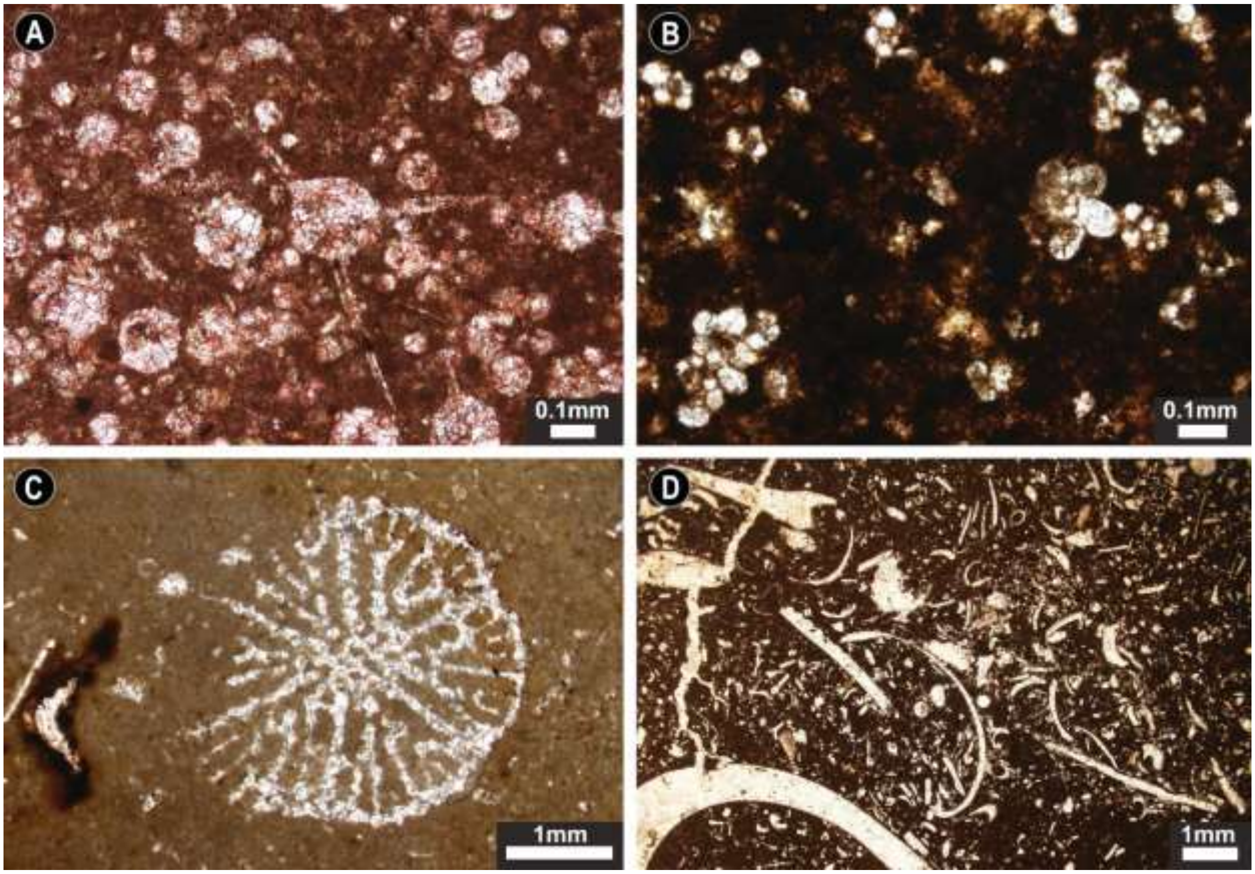

**Fig. 3.** Thin section photomicrographs of typical facies under plane-polarized light (PPL). (A) radiolarian wackestone-packstone, MF1. (B) planktonic foraminiferal wackestone, MF2. (C) Bioclast (coral) floatstone, MF3. (D) Bioclast packstone and rudstone, MF4.

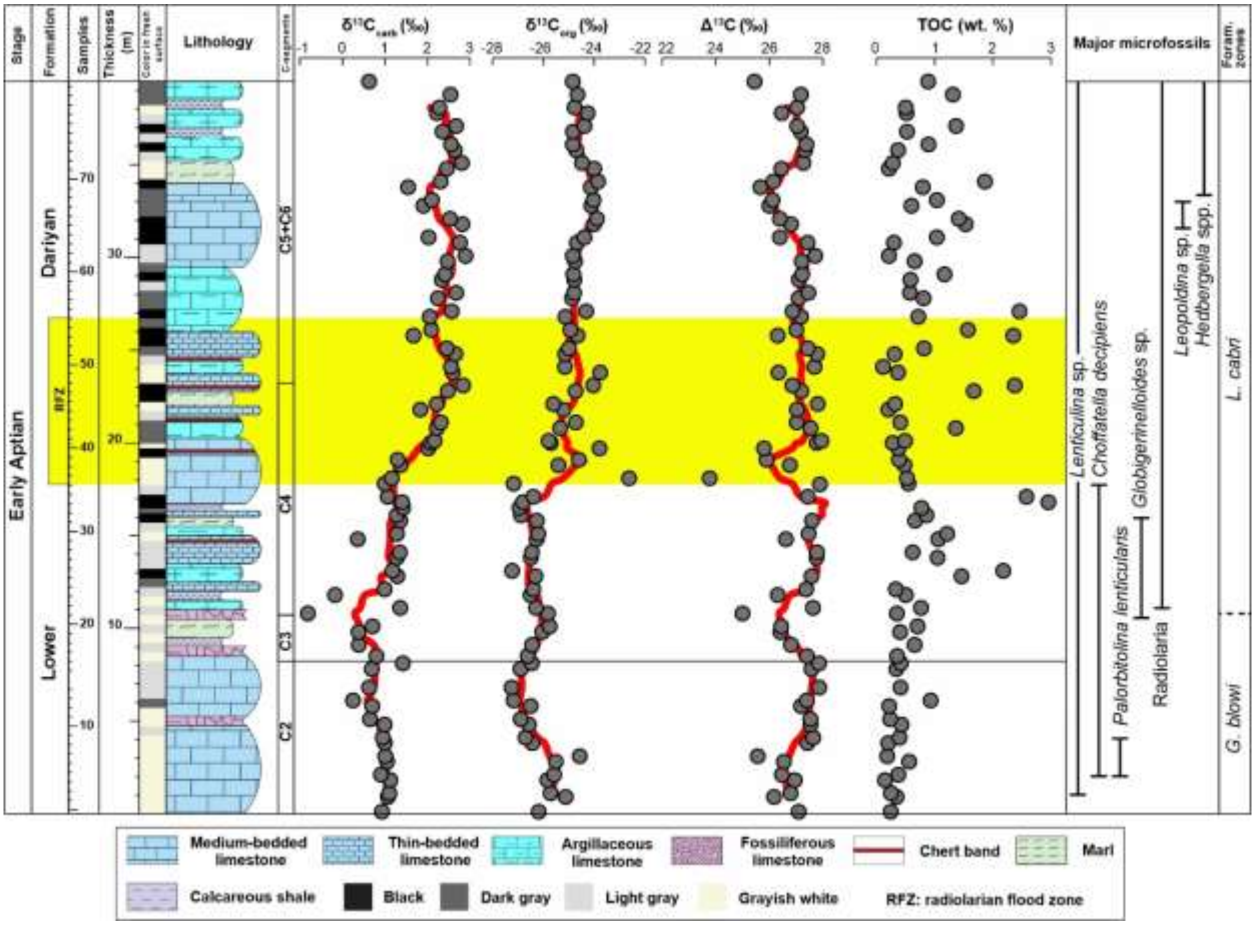

**Fig. 4.** Stratigraphic column of the Lower Dariyan unit at the Dareh Sefid section showing lithology, carbon-isotope stages *sensu* Menegatti et al. (1988), chemostratigraphy, TOC content, major microfossils, and planktic foraminifera biozonation. The radiolarian flood zone (RFZ) is highlighted in yellow. Thick red lines represent 5-point moving averages. $\delta^{13}C_{carb}$ data and major microfossils from Jafarian et al. (2023). Tethyan planktic formainifera biozones after Castro et al. (2021). For location of the Dareh Sefid section see Figure 1.

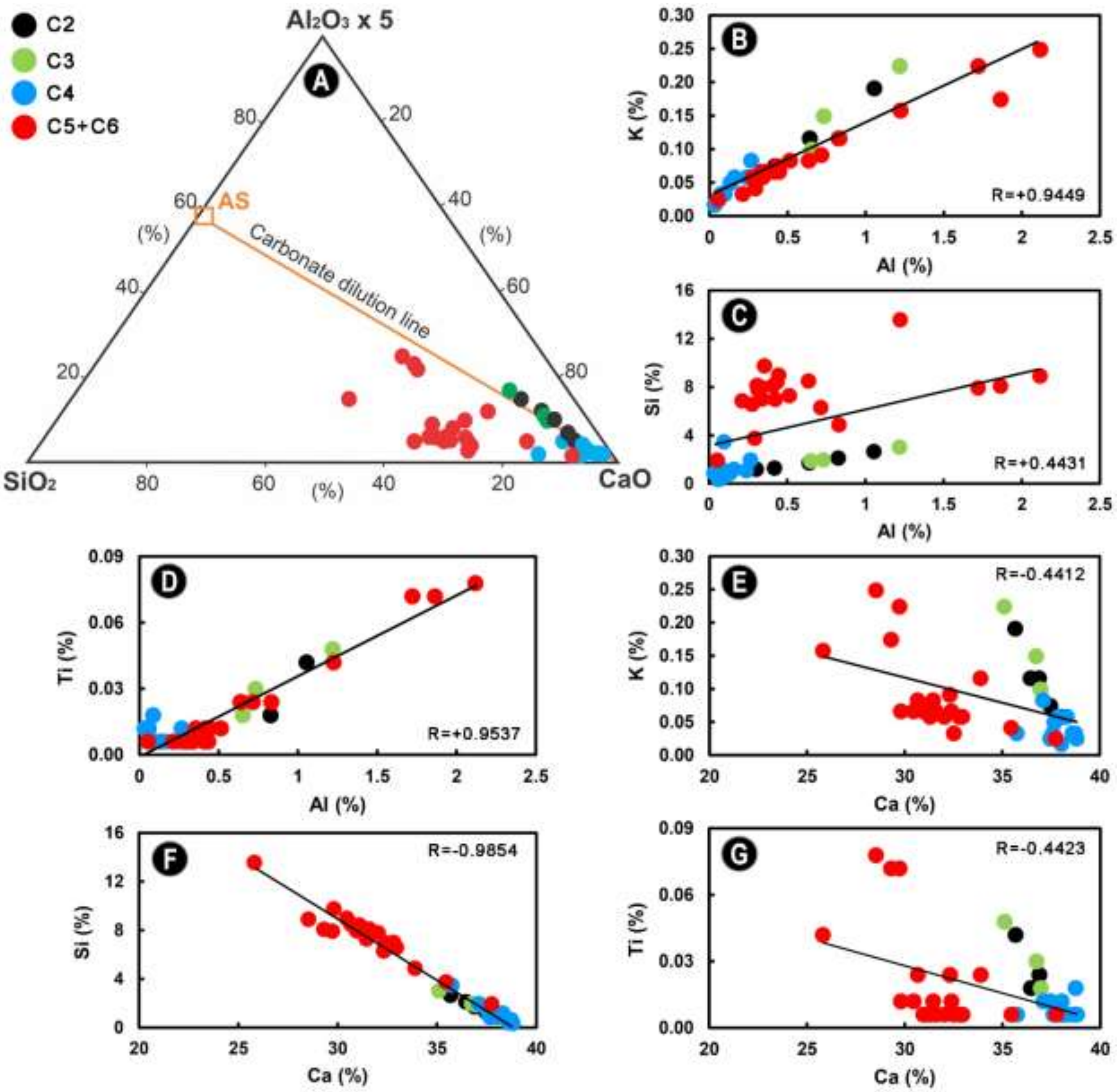

**Fig. 5.** (A) Ternary diagram shows the relative proportions of $Al_2O_3$ (multiplied by 5; representing clay minerals), $SiO_2$ (representing quartz or biogenic silica), and CaO (representing carbonate) for samples from the Dareh Sefid section. The average shale (AS) composition (Wedepohl, 1971, 1991) and the carbonate dilution line are also included for reference. (B-G) Cross plots of selected lithogenic conservative elements (K, Ti, and Si) versus Al and Ca concentrations.

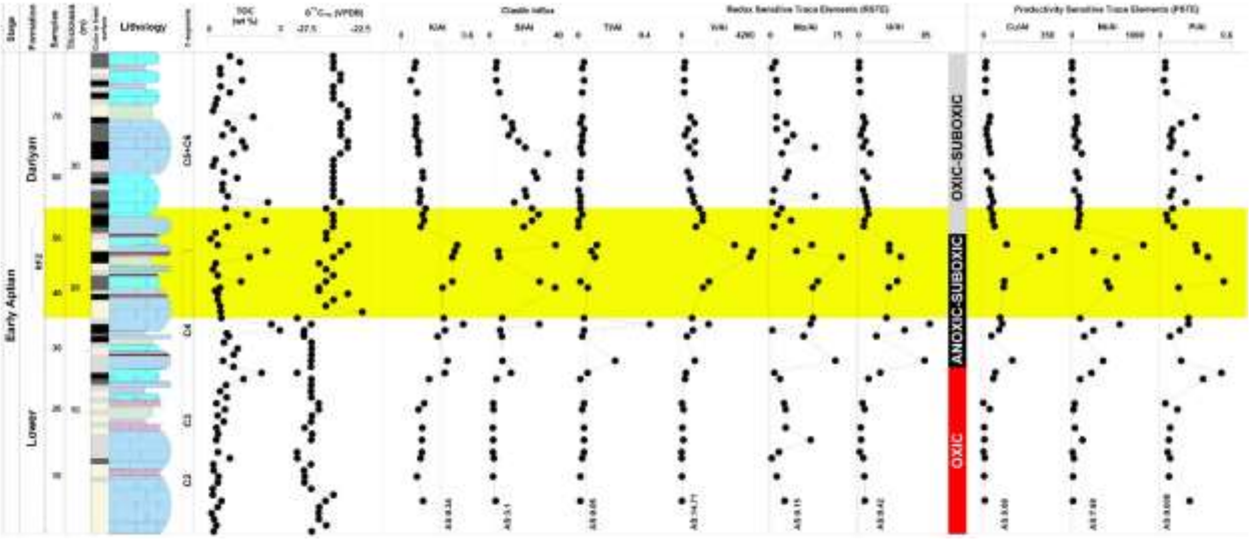

**Fig. 6.** The stratigraphic correlation of major and trace elements, TOC, and $\delta^{13}C_{org}$ which have been normalized to aluminum concentration, is paired with the subdivision of carbon isotope segments of Menegatti et al. (1988), in the Dareh Sefid section. The Al-normalized concentrations of each element in AS (Wedepohl, 1971, 1991) are shown by thin red lines.

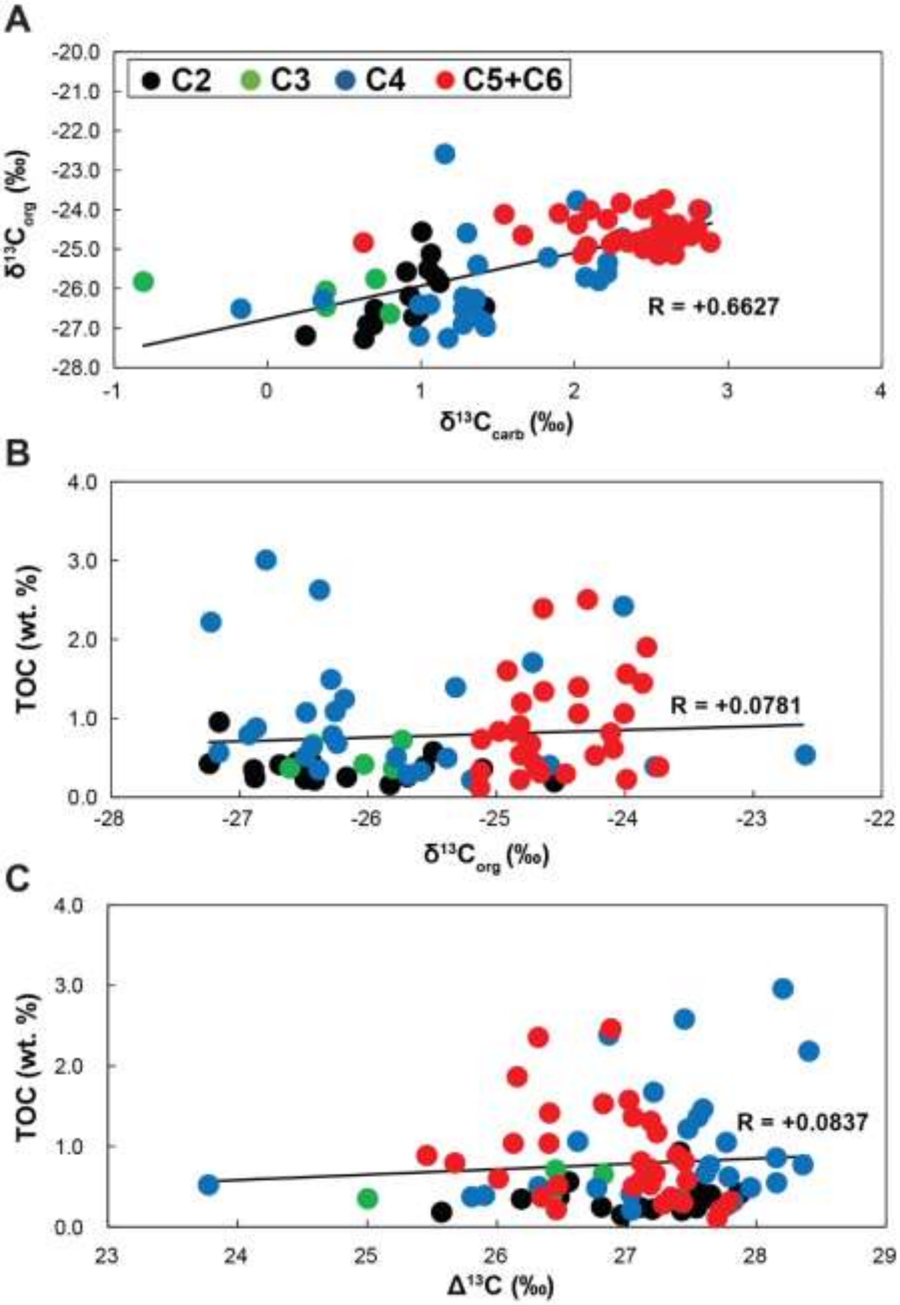

**Fig. 7.** Cross plots showing the relationships among organic ($\delta^{13}C_{org}$) and bulk carbonate ($\delta^{13}C_{carb}$) carbon isotopes, total organic carbon (TOC), and the isotopic difference between paired isotopic measurements of bulk carbonate and organic matter ($\Delta^{13}C = \delta^{13}C_{carb} - \delta^{13}C_{org}$).

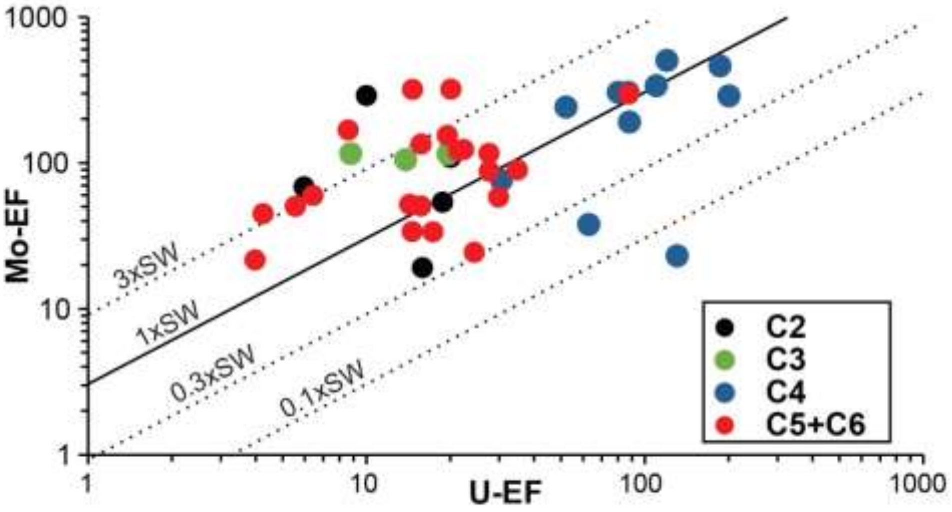

**Fig. 8.** Mo-EF versus U-EF for the Lower Aptian Lower Dariyan unit. Carbon isotope segments *sensu* Menegatti et al. (1988) after Jafarian et al. (2023). Sloping lines indicate Mo/U ratios equal to the seawater value (1x SW) and to the multiples (3x SW) and fractions thereof (0.1x SW, 0.3x SW).

## Supplementary Material

**Table S1.** $\delta^{13}$C and TOC data, Dareh Defid section, Lower Aptian Dariyan Formation, Fars Province, Iran.

**Table S2.** XRF and ICP-MS analysis data, Lower Aptian Dariyan Formation, Dareh Sefid section, Fars Province, Iran.

**Table S3.** Summary data of productive-sensitive (PSTE) and redox-sensitive trace elements (RSTE) normalized to Al and enrichment factors for U and Mo. Dareh Defid section, Lower Aptian Dariyan Formation, Fars Province, Iran.

Table S1. $\delta^{13}C$ and TOC data, Dareh Defid section, Lower Aptian Dariyan Formation, Fars Province, Iran.

| Sample no. | Stratigraphic position (m) | C segment | $\delta^{13}C_{carb}$ (‰VPDB) | $\delta^{13}C_{org}$ (‰VPDB) | $\Delta^{13}C$ (‰VPDB) | TOC (%) |
|---|---|---|---|---|---|---|
| DD 1 | 0.1 | C2 | 0.93 | -26.17 | 27.10 | 0.24 |
| DD 2 | 0.9 | C2 | 1.07 | -25.12 | 26.19 | 0.35 |
| DD 3 | 1.1 | C2 | 1.10 | -25.70 | 26.80 | 0.25 |
| DD 4 | 1.8 | C2 | 1.12 | -25.84 | 26.96 | 0.15 |
| DD 5 | 2.1 | C2 | 0.91 | -25.57 | 26.48 | 0.38 |
| DD 6 | 2.8 | C2 | 1.05 | -25.50 | 26.55 | 0.56 |
| DD 7 | 3.1 | C2 | 1.01 | -24.56 | 25.57 | 0.18 |
| DD 8 | 3.8 | C2 | 1.00 | -26.42 | 27.42 | 0.20 |
| DD 9 | 4.1 | C2 | 0.95 | -26.69 | 27.65 | 0.40 |
| DD 10 | 4.8 | C2 | 0.99 | -26.56 | 27.55 | 0.43 |
| DD 11 | 5.1 | C2 | 0.65 | -26.88 | 27.54 | 0.24 |
| DD 12 | 5.8 | C2 | 0.70 | -26.50 | 27.20 | 0.22 |
| DD 13 | 6.1 | C2 | 0.25 | -27.16 | 27.41 | 0.93 |
| DD 14 | 6.8 | C2 | 0.63 | -27.24 | 27.87 | 0.41 |
| DD 15 | 7.8 | C2 | 0.69 | -26.89 | 27.58 | 0.34 |
| DD 16 | 8.1 | C2 | 1.42 | -26.44 | 27.86 | 0.42 |
| DD 17 | 8.5 | C3 | 0.80 | -26.61 | 27.41 | 0.36 |
| DD 18 | 9.1 | C3 | 0.38 | -26.43 | 26.82 | 0.65 |
| DD 19 | 9.8 | C3 | 0.38 | -26.04 | 26.42 | 0.40 |
| DD 20 | 10.1 | C3 | 0.71 | -25.74 | 26.45 | 0.71 |
| DD 21 | 10.8 | C3 | -0.81 | -25.81 | 25.00 | 0.35 |
| DD 22 | 11.1 | C4 | 1.35 | -26.28 | 27.64 | 0.77 |
| DD 23 | 11.8 | C4 | -0.17 | -26.49 | 26.32 | 0.50 |
| DD 24 | 12.1 | C4 | 0.99 | -26.39 | 27.38 | 0.34 |
| DD 25 | 12.8 | C4 | 1.29 | -26.29 | 27.59 | 1.46 |
| DD 26 | 13.1 | C4 | 1.18 | -27.22 | 28.40 | 2.18 |
| DD 27 | 13.8 | C4 | 1.28 | -26.49 | 27.77 | 1.05 |
| DD 28 | 14.1 | C4 | 1.34 | -26.44 | 27.79 | 0.62 |
| DD 29 | 14.8 | C4 | 0.36 | -26.26 | 26.62 | 1.06 |
| DD 30 | 15.1 | C4 | 1.28 | -26.19 | 27.47 | 1.22 |
| DD 31 | 15.8 | C4 | 1.36 | -26.25 | 27.60 | 0.67 |
| DD 32 | 16.1 | C4 | 1.28 | -26.87 | 28.15 | 0.86 |
| DD 33 | 16.5 | C4 | 1.42 | -26.93 | 28.36 | 0.77 |
| DD 34 | 16.8 | C4 | 1.41 | -26.80 | 28.20 | 2.96 |
| DD 35 | 17.1 | C4 | 1.06 | -26.38 | 27.44 | 2.58 |
| DD 36 | 17.8 | C4 | 0.99 | -27.16 | 28.15 | 0.55 |
| DD 37 | 18.1 | C4 | 1.16 | -22.62 | 23.77 | 0.52 |
| DD 38 | 18.8 | C4 | 1.37 | -25.39 | 26.77 | 0.48 |
| DD 39 | 19.1 | C4 | 1.30 | -24.60 | 25.90 | 0.39 |
| DD 40 | 19.7 | C4 | 2.02 | -23.78 | 25.80 | 0.38 |

| | | | | | | |
|---|---|---|---|---|---|---|
| DD 41 | 20 | C4 | 2.08 | -25.70 | 27.78 | 0.28 |
| DD 42 | 20.1 | C4 | 2.16 | -25.79 | 27.95 | 0.49 |
| DD 43 | 20.8 | C4 | 2.22 | -25.33 | 27.55 | 1.36 |
| DD 44 | 21.1 | C4 | 2.32 | -24.71 | 27.03 | 0.41 |
| DD 45 | 21.8 | C4 | 1.83 | -25.20 | 27.04 | 0.21 |
| DD 46 | 22.1 | C4 | 2.22 | -25.60 | 27.82 | 0.32 |
| DD 47 | 22.8 | C4 | 2.48 | -24.73 | 27.21 | 1.68 |
| DD 48 | 23.1 | C4 | 2.83 | -24.03 | 26.86 | 2.38 |
| DD 49 | 23.8 | C5+C6 | 2.59 | -23.75 | 26.34 | 0.37 |
| DD 50 | 24.1 | C5+C6 | 2.55 | -25.14 | 27.69 | 0.11 |
| DD 51 | 24.8 | C5+C6 | 2.66 | -25.14 | 27.79 | 0.31 |
| DD 52 | 25.1 | C5+C6 | 2.45 | -24.99 | 27.44 | 0.82 |
| DD 53 | 25.8 | C5+C6 | 1.67 | -24.65 | 26.32 | 2.35 |
| DD 54 | 26.1 | C5+C6 | 2.09 | -24.93 | 27.01 | 1.57 |
| DD 55 | 26.8 | C5+C6 | 2.06 | -25.13 | 27.18 | 0.72 |
| DD 56 | 27.1 | C5+C6 | 2.57 | -24.31 | 26.88 | 2.46 |
| DD 57 | 27.8 | C5+C6 | 2.24 | -24.86 | 27.11 | 0.81 |
| DD 58 | 28.1 | C5+C6 | 2.67 | -24.79 | 27.46 | 0.58 |
| DD 59 | 28.8 | C5+C6 | 2.34 | -24.78 | 27.11 | 0.58 |
| DD 60 | 29.1 | C5+C6 | 2.41 | -24.82 | 27.23 | 1.17 |
| DD 61 | 29.8 | C5+C6 | 2.47 | -24.75 | 27.22 | 0.66 |
| DD 62 | 30.1 | C5+C6 | 2.89 | -24.83 | 27.72 | 0.21 |
| DD 63 | 30.8 | C5+C6 | 2.76 | -24.67 | 27.43 | 0.30 |
| DD 64 | 31.1 | C5+C6 | 2.02 | -24.37 | 26.40 | 1.04 |
| DD 65 | 31.8 | C5+C6 | 2.81 | -24.00 | 26.82 | 1.53 |
| DD 66 | 32.1 | C5+C6 | 2.53 | -23.88 | 26.40 | 1.42 |
| DD 67 | 32.8 | C5+C6 | 1.90 | -24.11 | 26.01 | 0.60 |
| DD 68 | 33.1 | C5+C6 | 2.10 | -24.02 | 26.12 | 1.04 |
| DD 69 | 33.8 | C5+C6 | 1.54 | -24.13 | 25.67 | 0.80 |
| DD 70 | 34.1 | C5+C6 | 2.31 | -23.85 | 26.15 | 1.87 |
| DD 71 | 34.8 | C5+C6 | 2.45 | -24.00 | 26.45 | 0.22 |
| DD 72 | 35.1 | C5+C6 | 2.80 | -24.48 | 27.28 | 0.28 |
| DD 73 | 35.8 | C5+C6 | 2.64 | -24.70 | 27.34 | 0.37 |
| DD 74 | 36.1 | C5+C6 | 2.55 | -24.84 | 27.39 | 0.89 |
| DD 75 | 36.8 | C5+C6 | 2.36 | -24.82 | 27.18 | 0.52 |
| DD 76 | 37.1 | C5+C6 | 2.67 | -24.38 | 27.05 | 1.37 |
| DD 77 | 37.8 | C5+C6 | 2.22 | -24.25 | 26.47 | 0.52 |
| DD 78 | 38.1 | C5+C6 | 2.28 | -24.77 | 27.05 | 0.50 |
| DD 79 | 38.8 | C5+C6 | 2.54 | -24.64 | 27.18 | 1.32 |
| DD 80 | 39.5 | C5+C6 | 0.63 | -24.83 | 25.46 | 0.89 |

Table S2. XRF and ICP-MS analysis data, Lower Aptian Dariyan Formation, Dareh Sefid section, Fars Province, Iran.

| Sample no. | Stratigraphic position (m) | C segment | XRF (%) | | | | | | ICP-MS (ppm) | | | | |
|---|---|---|---|---|---|---|---|---|---|---|---|---|---|
| | | | $Al_2O_3$ | CaO | $K_2O$ | $P_2O_5$ | $SiO_2$ | $TiO_2$ | Cu | Ni | Mo | U | V |
| DD 06 | 2.8 | C2 | 0.57 | 53.20 | 0.07 | 0.100 | 2.58 | 0.01 | 3.5 | 11.9 | 4.84 | 2.53 | 23 |
| DD 10 | 4.8 | C2 | 1.56 | 51.00 | 0.14 | 0.090 | 4.55 | 0.03 | 6.9 | 32.9 | 6.55 | 6.48 | 59 |
| DD 13 | 6.1 | C2 | 0.79 | 52.40 | 0.09 | 0.050 | 2.77 | 0.02 | 4.6 | 21.3 | 1.18 | 2.78 | 27 |
| DD 14 | 6.8 | C2 | 1.99 | 49.90 | 0.23 | 0.100 | 5.69 | 0.07 | 5.6 | 34.1 | 10.65 | 2.63 | 55 |
| DD 15 | 7.8 | C2 | 1.21 | 51.60 | 0.14 | 0.070 | 3.67 | 0.04 | 6.4 | 107.5 | 27.3 | 2.68 | 98 |
| DD 17 | 8.5 | C3 | 2.30 | 49.10 | 0.27 | 0.140 | 6.49 | 0.08 | 10.8 | 77.0 | 20.8 | 4.47 | 119 |
| DD 20 | 10.1 | C3 | 1.23 | 51.70 | 0.12 | 0.130 | 4.06 | 0.03 | 23.0 | 28.9 | 11.05 | 5.34 | 107 |
| DD 21 | 10.8 | C3 | 1.38 | 51.40 | 0.18 | 0.050 | 4.23 | 0.05 | 3.4 | 43.8 | 11.30 | 4.23 | 57 |
| DD 25 | 12.8 | C4 | 0.45 | 53.00 | 0.07 | 0.110 | 2.32 | 0.01 | 12.4 | 32.2 | 2.67 | 3.04 | 60 |
| DD 26 | 13.1 | C4 | 0.17 | 52.60 | 0.04 | 0.060 | 2.40 | 0.01 | 5.6 | 26.1 | 0.50 | 2.37 | 27 |
| DD 28 | 14.1 | C4 | 0.16 | 54.20 | 0.04 | 0.020 | 1.39 | 0.03 | 12.1 | 38.0 | 5.76 | 6.59 | 69 |
| DD 32 | 16.1 | C4 | 0.50 | 51.90 | 0.10 | 0.030 | 4.22 | 0.02 | 11.4 | 50.6 | 9.40 | 5.77 | 97 |
| DD 34 | 16.8 | C4 | 0.25 | 52.70 | 0.06 | 0.030 | 1.84 | 0.01 | 10.6 | 41.9 | 0.45 | 7.23 | 93 |
| DD 35 | 17.1 | C4 | 0.06 | 53.20 | 0.02 | 0.010 | 1.89 | 0.02 | 3.0 | 21.5 | 1.35 | 2.66 | 51 |
| DD 36 | 17.8 | C4 | 0.30 | 53.60 | 0.07 | 0.050 | 2.59 | 0.01 | 13.5 | 21.6 | 7.14 | 5.33 | 104 |
| DD 42 | 20.1 | C4 | 0.18 | 50.00 | 0.04 | 0.020 | 7.44 | 0.01 | 9.7 | 51.5 | 4.28 | 3.47 | 123 |
| DD 43 | 20.8 | C4 | 0.11 | 52.40 | 0.03 | 0.040 | 3.50 | 0.02 | 6.1 | 29.1 | 2.90 | 2.68 | 95 |
| DD 47 | 22.8 | C4 | 0.11 | 54.30 | 0.03 | 0.030 | 0.74 | 0.01 | 16.1 | 36.8 | 4.33 | 2.92 | 232 |
| DD 48 | 23.1 | C4 | 0.14 | 54.00 | 0.04 | 0.030 | 0.89 | 0.01 | 25.3 | 23.9 | 2.08 | 2.73 | 306 |
| DD 49 | 23.8 | C5+C6 | 0.10 | 52.80 | 0.03 | 0.020 | 4.17 | 0.01 | 6.1 | 52.9 | 2.32 | 1.94 | 164 |
| DD 52 | 25.1 | C5+C6 | 0.82 | 43.50 | 0.09 | 0.070 | 18.05 | 0.01 | 25.0 | 45.3 | 2.15 | 3.15 | 380 |
| DD 53 | 25.8 | C5+C6 | 0.63 | 43.30 | 0.08 | 0.030 | 17.07 | 0.01 | 16.0 | 39.5 | 7.57 | 2.72 | 420 |
| DD 54 | 26.1 | C5+C6 | 0.67 | 41.70 | 0.08 | 0.030 | 20.88 | 0.02 | 17.2 | 46.9 | 3.04 | 4.42 | 447 |
| DD 55 | 26.8 | C5+C6 | 0.52 | 46.10 | 0.07 | 0.040 | 14.08 | 0.01 | 10.2 | 31.3 | 3.56 | 3.18 | 294 |
| DD 56 | 27.1 | C5+C6 | 0.97 | 44.00 | 0.10 | 0.150 | 15.60 | 0.02 | 26.2 | 67.3 | 1.84 | 5.24 | 395 |
| DD 57 | 27.8 | C5+C6 | 0.64 | 45.90 | 0.07 | 0.040 | 15.00 | 0.01 | 14.0 | 39.8 | 15.95 | 2.85 | 239 |
| DD 58 | 28.1 | C5+C6 | 0.77 | 44.20 | 0.08 | 0.060 | 17.34 | 0.01 | 13.8 | 23.1 | 2.03 | 2.49 | 219 |
| DD 60 | 29.1 | C5+C6 | 0.58 | 43.80 | 0.07 | 0.130 | 17.43 | 0.01 | 13.2 | 36.0 | 5.25 | 3.54 | 172 |

| | | | | | | | | | | | | | |
|---|---|---|---|---|---|---|---|---|---|---|---|---|---|
| DD 61 | 29.8 | C5+C6 | 0.59 | 44.80 | 0.07 | 0.050 | 16.68 | 0.01 | 6.7 | 25.8 | 6.18 | 2.05 | 124 |
| DD 64 | 31.1 | C5+C6 | 0.40 | 45.50 | 0.04 | 0.060 | 14.68 | 0.01 | 8.2 | 33.1 | 2.79 | 3.09 | 169 |
| DD 65 | 31.8 | C5+C6 | 0.84 | 42.60 | 0.08 | 0.050 | 19.24 | 0.02 | 13.5 | 35.1 | 20.9 | 2.72 | 216 |
| DD 66 | 32.1 | C5+C6 | 0.80 | 45.30 | 0.08 | 0.060 | 14.94 | 0.02 | 12.1 | 46.4 | 7.71 | 3.96 | 349 |
| DD 67 | 32.8 | C5+C6 | 2.31 | 36.10 | 0.19 | 0.140 | 29.07 | 0.07 | 24.7 | 66.6 | 30.3 | 4.39 | 295 |
| DD 68 | 33.1 | C5+C6 | 1.20 | 42.90 | 0.10 | 0.090 | 18.22 | 0.04 | 12.4 | 40.0 | 4.87 | 3.80 | 266 |
| DD 69 | 33.8 | C5+C6 | 0.55 | 49.60 | 0.05 | 0.070 | 8.04 | 0.01 | 9.1 | 29.3 | 5.19 | 2.61 | 232 |
| DD 70 | 34.1 | C5+C6 | 1.35 | 45.20 | 0.11 | 0.280 | 13.51 | 0.04 | 26.3 | 60.9 | 5.33 | 4.69 | 397 |
| DD 74 | 36.1 | C5+C6 | 1.57 | 47.40 | 0.14 | 0.070 | 10.44 | 0.04 | 12.2 | 31.6 | 7.33 | 2.23 | 175 |
| DD 76 | 37.1 | C5+C6 | 3.52 | 41.00 | 0.21 | 0.090 | 17.31 | 0.12 | 28.9 | 45.9 | 13.85 | 4.33 | 402 |
| DD 78 | 38.1 | C5+C6 | 4.00 | 39.90 | 0.30 | 0.140 | 19.08 | 0.13 | 30.9 | 54.1 | 6.75 | 3.52 | 429 |
| DD 79 | 38.8 | C5+C6 | 3.25 | 41.60 | 0.27 | 0.110 | 16.96 | 0.12 | 29.8 | 43.2 | 11.35 | 3.06 | 417 |

Table S3. Summary data of productive-sensitive (PSTE) and redox-sensitive trace elements (RSTE) normalized to Al and enrichment factors for U and Mo. Dareh Defid section, Lower Aptian Dariyan Formation, Fars Province, Iran.

| Sample no. | Stratigraphic position (m) | C segment | K/Al | Si/Al | Ti/Al | P/Al | Mo/Al | U/Al | V/Al | Cu/Al | Ni/Al | EF U | EF Mo |
|---|---|---|---|---|---|---|---|---|---|---|---|---|---|
| DD 06 | 2.8 | C2 | 0.1926 | 3.9978 | 0.0199 | 0.2567 | 16.0424 | 8.3858 | 76.2344 | 11.6009 | 39.4430 | 20.0337 | 109.0796 |
| DD 10 | 4.8 | C2 | 0.1408 | 2.5761 | 0.0218 | 0.0844 | 7.9326 | 7.8478 | 71.4538 | 8.3565 | 39.8446 | 18.7484 | 53.9374 |
| DD 13 | 6.1 | C2 | 0.1787 | 3.0969 | 0.0287 | 0.0926 | 2.8220 | 6.6484 | 64.5706 | 11.0009 | 50.9390 | 15.8830 | 19.1879 |
| DD 14 | 6.8 | C2 | 0.1813 | 2.5255 | 0.0398 | 0.0735 | 10.1110 | 2.4969 | 52.2165 | 5.3166 | 32.3742 | 5.9651 | 68.7495 |
| DD 15 | 7.8 | C2 | 0.1815 | 2.6789 | 0.0374 | 0.0847 | 42.6261 | 4.1845 | 153.0167 | 9.9929 | 167.8499 | 9.9969 | 289.8347 |
| DD 17 | 8.5 | C3 | 0.1841 | 2.4923 | 0.0394 | 0.0891 | 17.0857 | 3.6718 | 97.7501 | 8.8714 | 63.2501 | 8.7719 | 116.1739 |
| DD 20 | 10.1 | C3 | 0.1530 | 2.9154 | 0.0276 | 0.1547 | 16.9729 | 8.2023 | 164.3527 | 35.3281 | 44.3906 | 19.5953 | 115.4065 |
| DD 21 | 10.8 | C3 | 0.2046 | 2.7073 | 0.0410 | 0.0530 | 15.4703 | 5.7911 | 78.0358 | 4.6548 | 59.9643 | 13.8349 | 105.1895 |
| DD 25 | 12.8 | C4 | 0.2440 | 4.5536 | 0.0252 | 0.3577 | 11.2098 | 12.7632 | 251.9050 | 52.0604 | 135.1890 | 30.4913 | 76.2205 |
| DD 26 | 13.1 | C4 | 0.3691 | 12.4693 | 0.0666 | 0.5164 | 5.5567 | 26.3389 | 300.0633 | 62.2354 | 290.0612 | 62.9237 | 37.7828 |
| DD 28 | 14.1 | C4 | 0.3921 | 7.6732 | 0.2124 | 0.1829 | 68.0144 | 77.8150 | 814.7553 | 142.8774 | 448.7058 | 185.9003 | 462.4615 |
| DD 32 | 16.1 | C4 | 0.3137 | 7.4546 | 0.0453 | 0.0878 | 35.5186 | 21.8024 | 366.5218 | 43.0758 | 191.1959 | 52.0859 | 241.5077 |
| DD 34 | 16.8 | C4 | 0.3764 | 6.5007 | 0.0453 | 0.1756 | 3.4007 | 54.6382 | 702.8150 | 80.1058 | 316.6446 | 130.5308 | 23.1231 |
| DD 35 | 17.1 | C4 | 0.5228 | 27.8221 | 0.3775 | 0.2439 | 42.5090 | 83.7584 | 1605.8946 | 94.4644 | 676.9948 | 200.0991 | 289.0385 |
| DD 36 | 17.8 | C4 | 0.3660 | 7.6253 | 0.0378 | 0.2439 | 44.9650 | 33.5663 | 654.9531 | 85.0179 | 136.0287 | 80.1901 | 305.7385 |
| DD 42 | 20.1 | C4 | 0.3486 | 36.5073 | 0.0629 | 0.1626 | 44.9231 | 36.4213 | 1291.0133 | 101.8116 | 540.5462 | 87.0105 | 305.4530 |
| DD 43 | 20.8 | C4 | 0.4278 | 28.1032 | 0.2059 | 0.5321 | 49.8085 | 46.0299 | 1631.6576 | 104.7696 | 499.8025 | 109.9656 | 338.6713 |
| DD 47 | 22.8 | C4 | 0.4278 | 5.9418 | 0.1030 | 0.3991 | 74.3692 | 50.1520 | 3984.6796 | 276.5230 | 632.0526 | 119.8133 | 505.6713 |
| DD 48 | 23.1 | C4 | 0.4481 | 5.6149 | 0.0809 | 0.3136 | 28.0694 | 36.8411 | 4129.4432 | 341.4213 | 322.5284 | 88.0135 | 190.8571 |
| DD 49 | 23.8 | C5+C6 | 0.4705 | 36.8312 | 0.1133 | 0.2927 | 43.8315 | 36.6522 | 3098.4319 | 115.2466 | 999.4332 | 87.5622 | 298.0308 |
| DD 52 | 25.1 | C5+C6 | 0.1722 | 19.4421 | 0.0138 | 0.1249 | 4.9536 | 7.2576 | 875.5236 | 57.6002 | 104.3716 | 17.3385 | 33.6820 |
| DD 53 | 25.8 | C5+C6 | 0.1992 | 23.9317 | 0.0180 | 0.0697 | 22.7014 | 8.1569 | 1259.5252 | 47.9819 | 118.4553 | 19.4869 | 154.3578 |
| DD 54 | 26.1 | C5+C6 | 0.1873 | 27.5255 | 0.0338 | 0.0655 | 8.5723 | 12.4637 | 1260.4651 | 48.5011 | 132.2501 | 29.7757 | 58.2870 |
| DD 55 | 26.8 | C5+C6 | 0.2111 | 23.9155 | 0.0218 | 0.1126 | 12.9344 | 11.5537 | 1068.1742 | 37.0591 | 113.7206 | 27.6019 | 87.9467 |
| DD 56 | 27.1 | C5+C6 | 0.1617 | 14.2047 | 0.0234 | 0.2263 | 3.5838 | 10.2060 | 769.3491 | 51.0302 | 131.0815 | 24.3823 | 24.3680 |
| DD 57 | 27.8 | C5+C6 | 0.1716 | 20.7010 | 0.0177 | 0.0915 | 47.0846 | 8.4132 | 705.5309 | 41.3282 | 117.4901 | 20.0992 | 320.1502 |
| DD 58 | 28.1 | C5+C6 | 0.1630 | 19.8902 | 0.0147 | 0.1140 | 4.9808 | 6.1095 | 537.3429 | 33.8600 | 56.6786 | 14.5956 | 33.8671 |

| | | | | | | | | | | | | | |
|---|---|---|---|---|---|---|---|---|---|---|---|---|---|
| DD 60 | 29.1 | C5+C6 | 0.1893 | 26.5429 | 0.0195 | 0.3280 | 17.1013 | 11.5312 | 560.2715 | 42.9976 | 117.2661 | 27.5480 | 116.2798 |
| DD 61 | 29.8 | C5+C6 | 0.1861 | 24.9703 | 0.0192 | 0.1240 | 19.7895 | 6.5645 | 397.0764 | 21.4546 | 82.6163 | 15.6825 | 134.5580 |
| DD 64 | 31.1 | C5+C6 | 0.1568 | 32.4150 | 0.0283 | 0.2195 | 13.1778 | 14.5947 | 798.2241 | 38.7304 | 156.3386 | 34.8669 | 89.6019 |
| DD 65 | 31.8 | C5+C6 | 0.1494 | 20.2304 | 0.0270 | 0.0871 | 47.0073 | 6.1177 | 485.8168 | 30.3636 | 78.9452 | 14.6152 | 319.6245 |
| DD 66 | 32.1 | C5+C6 | 0.1568 | 16.4945 | 0.0283 | 0.1097 | 18.2080 | 9.3520 | 824.2018 | 28.5755 | 109.5787 | 22.3419 | 123.8048 |
| DD 67 | 32.8 | C5+C6 | 0.1290 | 11.1151 | 0.0343 | 0.0887 | 24.7816 | 3.5905 | 241.2727 | 20.2015 | 54.4704 | 8.5776 | 168.5015 |
| DD 68 | 33.1 | C5+C6 | 0.1307 | 13.4106 | 0.0378 | 0.1097 | 7.6674 | 5.9827 | 418.7921 | 19.5226 | 62.9763 | 14.2928 | 52.1340 |
| DD 69 | 33.8 | C5+C6 | 0.1426 | 12.9114 | 0.0206 | 0.1862 | 17.8280 | 8.9655 | 796.9359 | 31.2591 | 100.6475 | 21.4187 | 121.2210 |
| DD 70 | 34.1 | C5+C6 | 0.1278 | 8.8390 | 0.0336 | 0.3035 | 7.4592 | 6.5635 | 555.5905 | 36.8061 | 85.2279 | 15.6803 | 50.7185 |
| DD 74 | 36.1 | C5+C6 | 0.1399 | 5.8733 | 0.0289 | 0.0652 | 8.8207 | 2.6835 | 210.5894 | 14.6811 | 38.0264 | 6.4109 | 59.9760 |
| DD 76 | 37.1 | C5+C6 | 0.0936 | 4.3434 | 0.0386 | 0.0374 | 7.4337 | 2.3240 | 215.7652 | 15.5115 | 24.6359 | 5.5521 | 50.5452 |
| DD 78 | 38.1 | C5+C6 | 0.1176 | 4.2131 | 0.0368 | 0.0512 | 3.1882 | 1.6626 | 202.6261 | 14.5947 | 25.5526 | 3.9719 | 21.6779 |
| DD 79 | 38.8 | C5+C6 | 0.1303 | 4.6092 | 0.0418 | 0.0495 | 6.5980 | 1.7788 | 242.4101 | 17.3233 | 25.1130 | 4.2496 | 44.8627 |

**Citation on deposit:** Jafarian, A., Husinec, A., Wang, C., Chen, X., Wang, M., Gröcke, D. R., …Li, Y. (2024). Intrashelf basin record of redox and productivity changes along the Arabian margin of Neo-Tethys during Oceanic Anoxic Event 1a. Palaeogeography, Palaeoclimatology, Palaeoecology, 636, Article 111975. https://doi.org/10.1016/j.palaeo.2023.111975